Advances in Colloid and Interface Science 168 (2011) 50–70

Contents lists available at ScienceDirect

Advances in Colloid and Interface Science

journal homepage: www.elsevier.com/locate/cis

The metastable states of foam films containing electrically charged micelles or particles: Experiment and quantitative interpretation ☆

Krassimir D. Danov [a], Elka S. Basheva [a], Peter A. Kralchevsky [a,*], Kavssery P. Ananthapadmanabhan [b], Alex Lips [c]

[a] Department of Chemical Engineering, Faculty of Chemistry, Sofia University, 1164 Sofia, Bulgaria
[b] Unilever Research & Development, 40 Merritt Blvd., Trumbull, Connecticut 06611, USA
[c] Unilever Research & Development, Port Sunlight, Wirral, Merseyside CH63 3JW, UK

ARTICLE INFO

Available online 12 April 2011

Keywords:
Charged particles in liquid films
Stepwise thinning of foam films
Degree of micelle ionization
Aggregation number of ionic micelles

ABSTRACT

The stepwise thinning (stratification) of liquid films containing electrically charged colloidal particles (in our case — surfactant micelles) is investigated. Most of the results are applicable also to films from nanoparticle suspensions. The aim is to achieve agreement between theory and experiment, and to better understand the physical reasons for this phenomenon. To test different theoretical approaches, we obtained experimental data for free foam films from micellar solutions of three ionic surfactants. The theoretical problem is reduced to the interpretation of the experimental concentration dependencies of the step height and of the final film thickness. The surface charges of films and micelles are calculated by means of the charge-regulation model, with a counterion-binding (Stern) constant determined from the fit of surface tension isotherms. The applicability of three models was tested: the Poisson–Boltzmann (PB) model; the jellium-approximation (JA), and the cell model (CM). The best agreement theory/experiment was obtained with the JA model without using any adjustable parameters. Two theoretical approaches are considered. First, in the energy approach the step height is identified with the effective diameter of the charged micelles, which represents an integral of the electrostatic-repulsion energy calculated by the JA model. Second, in the osmotic approach the step height is equal to the inverse cubic root of micelle number density in the bulk of solution. Both approaches are in good agreement with the experiment if the suspension of charged particles (micelles) represents a jellium, i.e. if the particle concentration is uniform despite the field of the electric double layers. The results lead to a convenient method for determining the aggregation number of ionic surfactant micelles from the experimental heights of the steps.

1. Introduction

Stepwise thinning of foam films was observed long ago by Johonnott [1] and Perrin [2], and this phenomenon was called *stratification* [2]. It was explained as a layer-by-layer pressing out of spherical colloid particles, e.g. surfactant micelles or latex beads, contained in the film [3–8]; see Fig. 1. The latter give rise to an oscillatory force between the film surfaces, which was directly detected by the porous-plate-cell method [9,10] and surface-force apparatus [11,12]. Physically, this force is analogous to the oscillatory structural force detected in organic liquids [13,14] and in aqueous solutions [15,16] confined between two smooth solid surfaces. In the latter case, the structural units are molecules of the liquid rather than dispersed colloid particles. The colloid structural forces can stabilize liquid films and disperse systems, since they hamper the film drainage [7,8,17–20]. Their effect was studied by light-scattering method [21]; by electron cryomicroscopy [22,23]; by colloidal-probe atomic-force microscopy (CP-AFM) [24–38]; in foam and emulsion films [19,39–42], in asymmetric and wetting films [43–46]. Such forces are observed also in more complex systems like protein solutions, surfactant–polymer mixtures, solutions of polyelectrolytes and amphiphilic block copolymers; for recent reviews see [19,20,47].

The developed theories are based on modeling by means of the integral equations of statistical mechanics [34,35,48–51] and numerical simulations [34–37,52–58]. As a rule, these approaches are related to complicated theoretical expressions or numerical procedures. To overcome this difficulty, for the case of uncharged particles some relatively simple semiempirical expressions have been proposed [59,60] on the basis of fits of theoretical results for hard-sphere fluids. In recent studies, such a model was applied to determine the micelle aggregation number from the experimental step-wise transitions in the thickness of foam films [19], and to interpret the branches of the oscillatory structural force detected by CP-AFM [38].

☆ This article is dedicated to the memory of Prof. Nikolai V. Churaev, one of the pioneers in the field of surface forces and wetting films.

* Corresponding author.
E-mail address: pk@lcpe.uni-sofia.bg (P.A. Kralchevsky).

0001-8686/$ – see front matter © 2011 Elsevier B.V. All rights reserved.
doi:10.1016/j.cis.2011.03.006

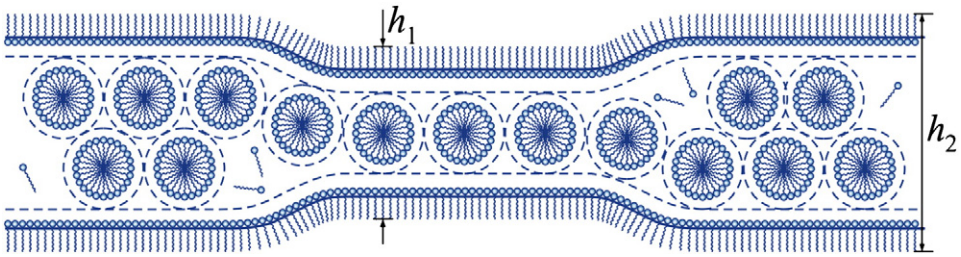

Fig. 1. Sketch of a foam film formed from a micellar solution of an ionic surfactant. The double electric layers around the micelles and near the film surfaces are denoted by dashed lines; h_1 and h_2 are the thicknesses in metastable states with one and two micellar layers inside the film.

For uncharged particles (e.g. nonionic micelles), the height of the stratification step, Δh, is approximately equal to the diameter of the hard sphere, slightly decreasing with the rise of the particle volume fraction [59,60]. Note that Δh coincides with the period of the oscillatory structural force. However, the studies on stratification with ionic micelles showed that the height of the step is considerably greater than the micelle hydrodynamic diameter, d_H. The first proposed estimate is $\Delta h = d_H + 2\kappa^{-1}$ [4], where the inverse Debye parameter κ^{-1} characterizes the thickness of the counterion atmosphere around the micelle. Despite being quantitatively inaccurate (see below), this first estimate correctly identifies the physical reason for the larger values of Δh for charged particles.

Another interesting finding is that the step height, Δh, is practically equal to the mean distance between the micelles in the bulk, δ_l, that is $\Delta h = \delta_l \equiv (c_{p\infty})^{-1/3}$, where $c_{p\infty}$ is the bulk micelle (particle) concentration [3,4]. This finding was utilized to construct the first simplified model of the stepwise transitions in stratifying films [5] using the interaction energy expression in the framework of the jellium-approximation [61,62]. Later, the fact that $\Delta h = (c_{p\infty})^{-1/3}$ was confirmed in experiments with charged nanoparticles and Monte Carlo (MC) simulations [26,27,35,36]. Henderson and Wasan et al. [54,55,63] carried out MC simulations of ionic micelle structuring in thin films and macroion layering in a wedge film and investigated the roles of electrostatics and excluded-volume effects. Klapp and von Klitzing et al. [34–37] combined MC simulations with CP-AFM measurements and small-angle neutron-scattering (SANS) to detect the structuring in the bulk and in narrow slits and to investigate the effects of charged walls [58].

Despite the achievements in this field and the accumulated results from experiments and numerical simulations, analytical expressions that describe the oscillatory structural force in the case of charged particles are still missing. Here, our goal is to develop an analytical theory that explains the step height, Δh, and the final film thickness, h_0, for stratifying films that contain charged particles. To test for different models in comparison with experimental data, we carried out systematic measurements with stratifying films from micellar solutions of three different ionic surfactants. To determine the charge of the micelles and film surfaces, electrolytic-conductivity and surface-tension measurements were also performed. After that, three possible theoretical models were tested, and it was found that one of them is in excellent agreement with the experimental data for h_0 and Δh. A theoretical expression for the effective diameter of the charged micelles is proposed. The results indicate in what concentration domain the films with charged particles stratify and lead to a convenient method for determining the aggregation number of ionic micelles from the stratification step height.

2. Materials and methods

In our experiments, the charged nano-sized particles are micelles of ionic surfactants. The working surfactant concentrations are ≤100 mM, where the micelles are spherical and relatively monodisperse. Three different ionic surfactants have been used: sodium dodecyl sulfate (SDS, anionic); cetyltrimethylammonium bromide (CTAB, cationic) and cetylpyridinium chloride (CPC, cationic); see Fig. 2. The purity of the used surfactants is 99%. The working temperature was 25 °C in all experiments. To prepare all solutions, deionized water (Milli-Q purification system, Millipore, USA) of specific resistivity 18.2 MΩ cm was used.

The used SDS ($C_{12}H_{25}SO_4Na$, CAS 151-21-3, molecular mass of 288.38 g/mol) was a product of Across Organics. At 25 °C, the critical micelle concentration (CMC) of SDS measured in different studies [64–70] is in the range of 7.6–8.3 mM in the absence of added electrolyte. Under the same conditions, the micellar aggregation number N_{agg} increases from 49 to 71 when the SDS concentration rises from 8 to 80 mM [69]. The outer (hydrodynamic) diameter of the smallest spherical SDS micelles is $d_H = 4.6$ nm [71–73]. The same value can be obtained by molecular-size considerations setting d_H equal to the doubled length of the SDS molecule. Thus, using the Tanford formula [74,75], for SDS we obtain:

$$(d_H)_{SDS} = 2\times(0.154 + 0.1265\times 12 + 0.3\times 2) = 4.544 \text{ (nm)} \qquad (2.1)$$

where 12 is the number of C atoms in the paraffin tail and 0.3 nm is the radius of the sulfate headgroup [65,76]. Note that at higher concentrations of added salt (>0.1 M), SDS exhibits the tendency to form elongated micelles, which can be modeled as sphero-cylinders of cross-sectional diameter ≈4.6 nm [72,73].

The used CTAB ($C_{16}H_{33}N(CH_3)_3Br$, CAS number 57-09-0, molecular mass 364.45 g/mol) was a product of Sigma. At 25 °C, the CMC of CTAB is in the range of 0.83–1.0 mM [77–85] in the absence of added electrolyte. The mean aggregation number of the CTAB micelles is $N_{agg} = 95$ [77,78]. A reasonable estimate of the micelle diameter can be made if we take the doubled length of the CTAB molecule:

$$(d_H)_{CTAB} = 2\times(0.154 + 0.1265\times 16 + 0.347\times 2) = 5.744 \approx 5.7 \text{ (nm)}. \qquad (2.2)$$

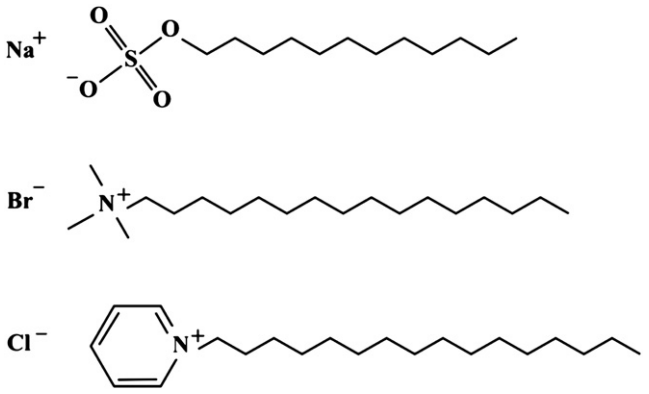

Fig. 2. Structural formulas of the used three ionic surfactants: sodium dodecyl sulfate (SDS), cetyltrimethylammonium bromide (CTAB), and cetylpyridinium chloride (CPC).

Here, the Tanford formula [74,75] was used to estimate the length of the C_{16} paraffin tail; the value 0.347 stands for the radius of the tetramethyl-ammonium ion [16].

The used CPC ($C_{21}H_{38}NCl$, CAS number 123-03-5, molecular mass 339.99 g/mol) was a product of Sigma. At 25 °C, the CMC of CPC is in the range of 0.887–1.24 mM [82,86–89] in the absence of added electrolyte. The aggregation number of the CPC micelles was found to vary in the range of $N_{agg}=45$–92 at low concentrations of added salt [87], and $N_{agg}=87$–120 at different surfactant concentrations [90]. For this surfactant, the most popular technique for determining micellar aggregation numbers, the static fluorescence quenching method, is inapplicable, because CPC is a good quencher of fluorescence. In the present study, comparing the calculated degree of micelle ionization with that determined by electrolytic conductivity measurements, we obtained $N_{agg}\approx 78$ for CPC (see below). As above, an estimate of the micelle diameter can be made if we take the doubled length of the CPC molecule:

$$(d_H)_{CPC}=2\times(0.154+0.1265\times 16+0.07+0.67)=5.836\approx 5.8\ \text{(nm)}. \tag{2.3}$$

Here, the Tanford formula [74,75] was used again to estimate the length of the C_{16} paraffin tail; the value 0.07 nm stands for the link between the paraffin chain and the pyridinium ring [16]; the diameter of the latter is estimated by using the diameter of the benzene ring, 0.67 nm [91].

Here, we are using the term "degree of ionization" of a micelle (or nanoparticle) as a term different from "degree of dissociation" [77,79]. For example, the sulfate groups on the surface of an SDS micelle are 100% dissociated. However, the ionization degree is only about 57% (see below) because of the binding (condensation) of hydrated Na^+ ions in the Stern layer, which leads to a fractional neutralization of the surface charge.

The Scheludko–Exerowa (SE) cell [92,93] was applied to study the stepwise thinning of individual free foam films. The procedure is as follows. First, the investigated solution is loaded in a cylindrical capillary (of an inner radius of 1.5 mm) through an orifice in its wall. Thus, a biconcave drop is formed inside the capillary. Next, liquid is sucked through the orifice and the two menisci approach each other until a film is formed in the central part of the cell. By injecting or sucking liquid through the orifice, one can vary the radius of the formed film, in which thickness can be measured by means of an interferometric method [93] of accuracy ±0.5 nm [9]. For this purpose, the light reflected from the film is supplied to a photomultiplier and computer, and the film thickness, h, is recorded as a function of time, t. The SE cell is placed in a closed container so that the water vapors are equilibrated with the solution, and evaporation from the film is prevented. For more details see e.g. [4,19].

To determine the electric charge of the micelles, we measured also the electrolytic conductivity of the solutions as a function of surfactant concentration by means of a conductivity-meter, Denver Instruments, USA. Surface tension isotherms were obtained by using the Wilhelmy plate method with tensiometer Krüss 10ST.

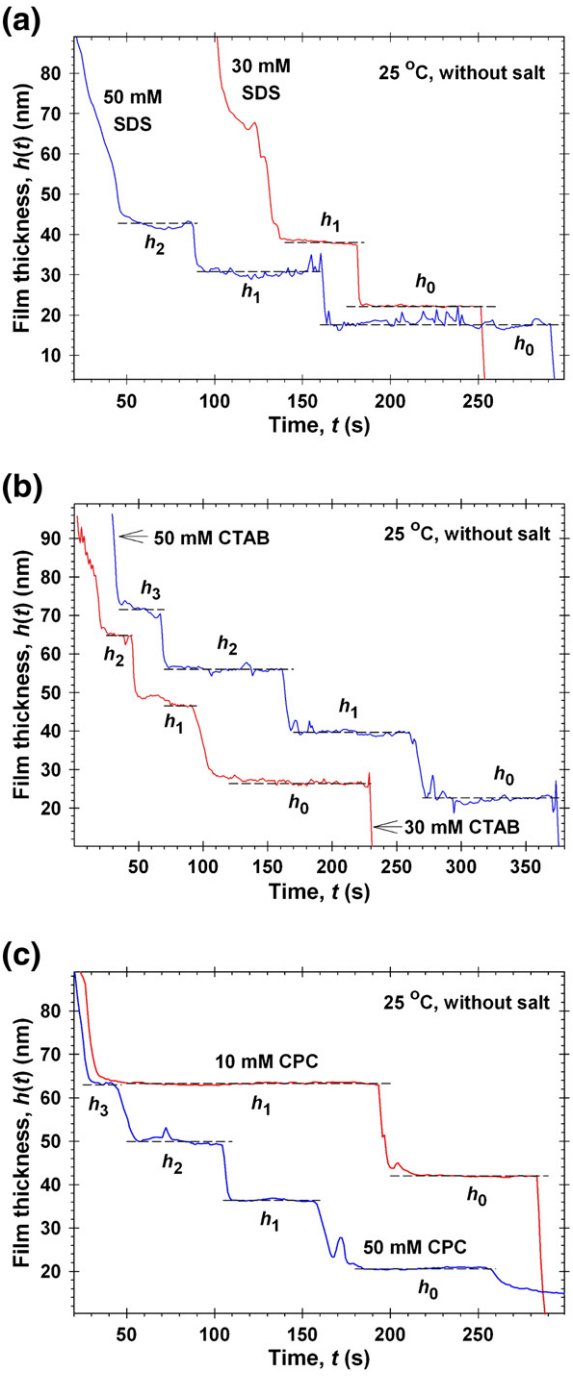

Fig. 3. Experimental time dependence, $h(t)$, of the equivalent water thickness of foam films in a SE cell: a) 30 mM and 50 mM SDS; b) 30 mM and 50 mM CTAB; and c) 10 mM and 50 mM CPC. h_3, h_2, h_1, and h_0 are the thicknesses in metastable states with three, two, one and zero micellar layers inside the film.

3. Experimental results and discussion

3.1. Results for stratifying foam films

Fig. 3 shows the typical experimental dependences of the film thickness, h, on time, t, obtained by means of an SE cell. The films are formed from micellar solutions of SDS (Fig. 3a), CTAB (Fig. 3b) and CPC (Fig. 3c) without added inorganic electrolyte (salt). As seen in the figures, h decreases with time by step-wise transitions. The transitions occur through the appearance and expansion of darker spots in the film. As already mentioned, the step-wise transitions were interpreted as a layer-by-layer thinning of an ordered structure of spherical particles inside the film [3–5]. In Fig. 3, the thicknesses of the films that contain 0, 1, 2 and 3 layers of micelles are denoted h_0, h_1, h_2 and h_3, each of them corresponding to a metastable state of the film. As seen in the figure, the number of observed metastable states (steps) increases with the rise of surfactant concentration.

In Fig. 4, we present experimental data for the dependence of h_0, h_1, h_2 and h_3 on the surfactant concentration. Each experimental point represents the mean value of 30 experiments. One sees that at a fixed surfactant concentration, the distances between the curves are the same, $h_1-h_0\approx h_2-h_1\approx\ldots\approx\Delta h$. The height of the step is

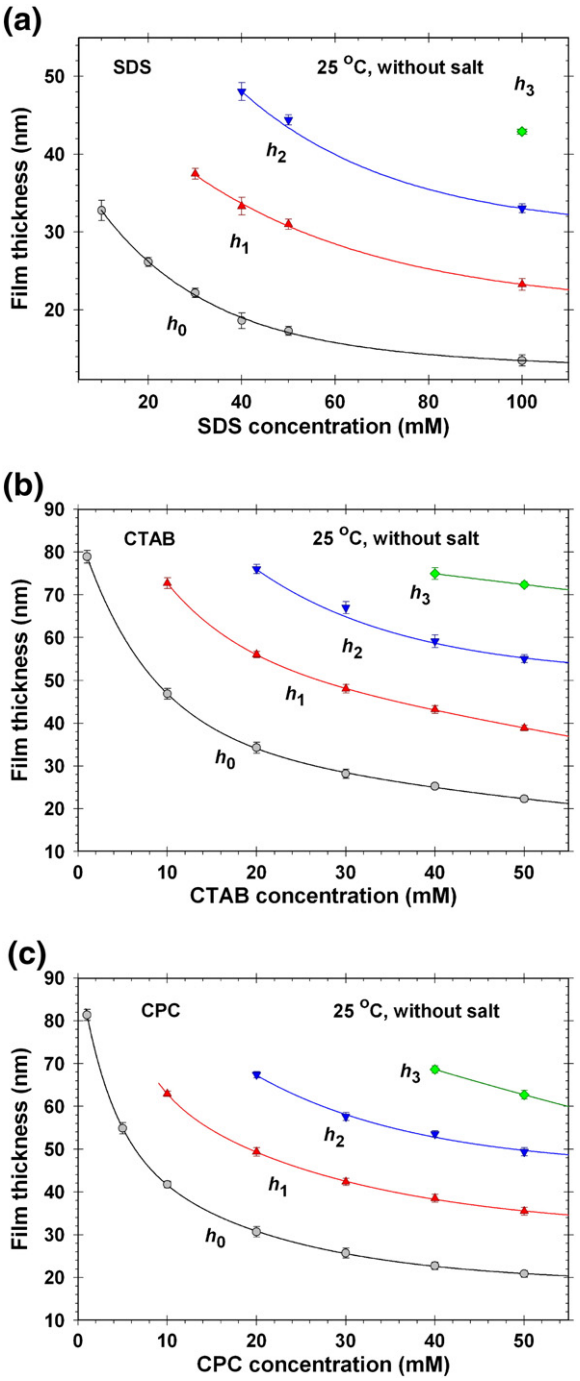

Fig. 4. The experimental film thickness h_n in the metastable states (with $n = 0, 1, 2$, and 3 layers of micelles in the film) vs. the surfactant concentration, c_s: a) SDS; b) CTAB; and c) CPC. The lines are guides to the eye.

considerably greater than the micelle hydrodynamic diameter. This situation ($\Delta h > d_H$) is similar for all studied surfactants and concentrations, which means that the electrostatic repulsion between the micelles gives an essential contribution to the heights of the steps [3–5]. As already mentioned, our aim in the present article is to give a quantitative interpretation of the experimental curves in Fig. 4, including the electrostatic contribution to the height of the steps, Δh, and the effect of micelle osmotic pressure on h_0.

Fig. 4 shows that h_i ($i = 0,1,2,\ldots$) decreases with the rise of surfactant concentration. Because the ionic surfactant is an electrolyte, a natural explanation of the latter fact is that the counterion atmospheres around the micelles shrink with the rise of the solution's ionic strength. In first approximation, the charged micelles could be modeled as hard spheres of effective diameter d_{eff} [4]:

$$d_{eff} = d_H + 2\kappa^{-1} \tag{3.1}$$

where d_H is the hydrodynamic diameter of the micelle and κ^{-1} is the Debye length that characterizes the thickness of the counterion atmosphere around the micelle. In the case of micellar solutions or suspensions of charged nanoparticles, not only the background electrolyte, but also the counterions dissociated from the micelles/particles contribute to κ. Beresford-Smith et al. [61,62] obtained the expression:

$$\kappa^2 = \kappa_0^2 + \kappa_{counterions}^2 \tag{3.2}$$

where κ_0 is the contribution of the background electrolyte. In the case of an ionic-surfactant micellar solution (without added salt), the concentration of background electrolyte is equal to the concentration of surfactant monomers that are in equilibrium with the micelles, i.e. to the critical micellization concentration, CMC. Then, Eq. (3.2) acquires the form:

$$\kappa^2 = 8\pi L_B\left[\mathrm{CMC} + \frac{\alpha}{2}(c_s - \mathrm{CMC})\right],\ L_B \equiv \frac{e^2}{\varepsilon kT}. \tag{3.3}$$

Here, c_s is the total surfactant concentration; k is the Boltzmann constant; T is the temperature; ε is the dielectric constant of water; e is the elementary electric charge; L_B is the Bjerrum length ($L_B = 0.72$ nm for water at 25 °C), and α is the degree of micelle ionization; α expresses the fraction of the surface ionic groups that are not neutralized by bound counterions.

To check whether we can model a charged particle (micelle) as an effective hard sphere that comprises the particle and its counterion atmosphere, in Eq. (3.1) we have set $d_{eff} \approx \Delta h$ and plot Δh vs. κ^{-1}, where Δh is experimentally determined and κ is calculated from Eq. (3.3). The results for SDS, CTAB and CPC are shown in Fig. 5, where the data are fitted with a linear regression

$$\Delta h = b_0 + b_1\kappa^{-1}. \tag{3.4}$$

Fig. 5 shows again that the height of the step, Δh, is considerably greater than the hydrodynamic diameter, d_H, of the respective micelles. Indeed, for SDS, CTAB and CPC the values of d_H are 4.6, 5.7 and 5.8 nm, respectively (see Section 2), whereas in Fig. 5 the experimental Δh has maximal values of 15.3, 25.9 and 21.2 nm for the same surfactants. In other words, the maximal Δh can be from 3.3 to 4.5 times greater than the micelle hydrodynamic diameter! This fact

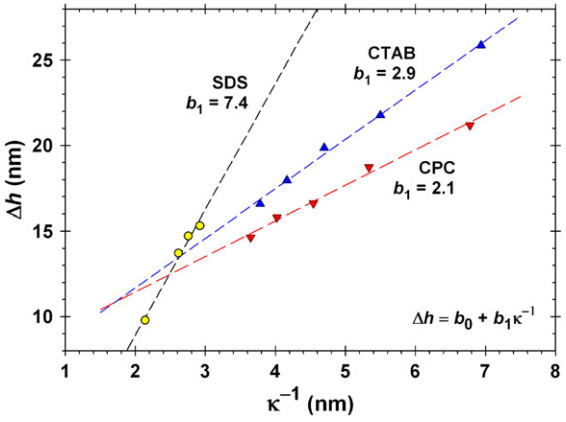

Fig. 5. The experimental height of the steps, Δh, plotted vs. the Debye screening length, κ^{-1}. The data for each surfactant are fitted by linear regression in accordance with Eq. (3.4); the parameters of the fits are given in Table 1.

indicates the existence of a very strong effect of the intermicellar electrostatic repulsion on the magnitude of the stratification steps. One of our main goals is to give a quantitative explanation of this effect.

The coefficients in Eq. (3.4) determined from the linear-regression fits in Fig. 5 are collected in Table 1, where the last column gives the references, from where the values of CMC and α have been taken to calculate κ from Eq. (3.3).

If Eq. (3.1) was valid, then b_0 should be equal to the micelle hydrodynamic diameter, d_H, whereas b_1 should be equal to 2. For CPC, b_1 is really close to 2, but b_0 is with 1.5 nm greater than d_H. The situation is the worst for SDS, for which $b_1 = 7.4$, and b_0 is even negative. Hence, we can conclude that Eq. (3.1) cannot be used as a basis of a quantitative model of the step-wise transitions.

An additional source of uncertainty is the value of the degree of ionization of the micelles, α. Depending on the used experimental method, rather different values of α have been obtained; see e.g. Table 1 in Ref. [64]. For example, for SDS micelles $\alpha = 0.14$ was obtained by electromotive-force measurements of the activity of Na^+ ions [95], whereas $\alpha = 0.54$ was determined from the dependence of CMC on the Na^+ concentration [96,97]. Low values, $\alpha = 0.05$ for SDS micelles and 0.08 for CPC micelles, were obtained by theoretical analysis of data for the solutions' osmotic pressure [90]. To be certain about the value of α, we employed additional surface tension and conductivity data (see Sections 3.2 and 3.3). From the surface-tension data, the Stern constant K_{St} can be determined, which characterizes the binding of counterions to the ionic headgroups of the surfactant molecules. Using the determined K_{St}, we can further calculate α for micelles (Section 4) and compare the obtained results with α independently determined from conductivity (Section 3.3).

3.2. Surface tension isotherms and determination of the stern constant

To determine K_{St} with a good precision, we have to process surface tension data obtained at *several* different salt concentrations [98]. In Fig. 6, such experimental curves are shown for CPC at 0, 10, 20 and 100 mM added NaCl. The curve obtained in the absence of NaCl is from Ref. [87], whereas the other three curves have been obtained by us. The data are fitted with the help of the van der Waals model. The best fit is shown by solid line in Fig. 6. The theoretical dependence of the surface tension, σ, on the surfactant and salt concentrations is calculated as follows:

The van der Waals adsorption isotherm for an *ionic* surfactant can be expressed in the form [98,99]:

$$(1+K_{St}a_{2s})K_1a_{1s} = \frac{\Gamma_1}{\Gamma_\infty-\Gamma_1}\,exp\left(\frac{\Gamma_1}{\Gamma_\infty-\Gamma_1}-\frac{2\beta\Gamma_1}{kT}\right) \tag{3.5}$$

where Γ_1 is the surfactant adsorption at the air/water interface; Γ_∞ is the maximal value of Γ_1 at saturation; β is a constant parameter that characterizes the interaction between the adsorbed surfactant molecules; K_1 is the surfactant adsorption parameter, which is related to the adsorption energy per molecule; a_{1s} and a_{2s} are the subsurface activities of the surfactant ions and counterions, which are related to the respective bulk concentrations $c_{1\infty}$ and $c_{2\infty}$ by means of the Boltzmann equation:

$$a_{1s} = \gamma_\pm c_{1\infty}\,exp(-\Phi_s), \quad a_{2s} = \gamma_\pm c_{2\infty}\,exp\Phi_s \tag{3.6}$$

Table 1
Verification of Eq. (3.1) with $\Delta h = d_{eff}$; see Fig. 5.

Surfactant	CMC (mM)	α	b_0 (nm)	b_1	References
SDS	8.0	0.27	−5.8	7.4	[4,68,70,94]
CTAB	0.9	0.23	5.9	2.9	[11,78,94]
CPC	0.9	0.20	7.3	2.1	[88]

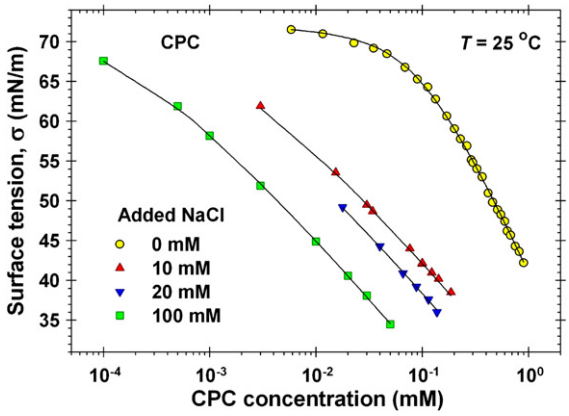

Fig. 6. Surface tension of CPC solutions vs. the CPC concentration at four concentrations of added NaCl; $T = 25$ °C. The isotherm without NaCl is from Ref. [87], whereas the isotherms with 10, 20 and 100 mM NaCl have been obtained by us. The solid lines are the best theoretical fits, in which parameters are given in Table 2 (the last row).

where $\gamma_\pm$ is the activity coefficient estimated from the Debye–Hückel theory as explained in Ref. [99]; $\Phi_s = (ze\psi_s)/(kT)$ is the dimensionless surface electric potential; $z = +1$ and -1, respectively, are for positively and negatively charged surface of potential ψ_s. To close the system of equations, we have to use also the Gouy equation that connects the surface charge and potential,

$$\Gamma_1 - \Gamma_2 = \left(\frac{2c_{2\infty}}{\pi L_B}\right)^{1/2} sinh\left(\frac{\Phi_s}{2}\right) \tag{3.7}$$

and the Stern isotherm of counterion adsorption (binding):

$$\frac{\Gamma_2}{\Gamma_1} = \frac{K_{St}a_{2s}}{1+K_{St}a_{2s}} \tag{3.8}$$

with Γ_2 being the surface density of counterions, which are bound (adsorbed) in the Stern layer. Note that $c_{2\infty} = c_{1\infty} + c_{3\infty}$, where $c_{1\infty}$, $c_{2\infty}$ and $c_{3\infty}$ are the bulk concentrations of surfactant ions, counterions and added salt. Eqs. (3.5)–(3.8) represent a system of 5 equations for determining the 5 unknown variables, Γ_1, Γ_2, a_{1s}, a_{2s} and Φ_s, at every given surfactant and salt concentrations, $c_{1\infty}$ and $c_{3\infty}$. The principles of the numerical procedure for solving this system of equations are described in Ref. [99]. After solving the above system of equations, the surface tension is calculated from the expression [99]:

$$\frac{\sigma_0-\sigma}{kT} = \frac{\Gamma_\infty\Gamma_1}{\Gamma_\infty-\Gamma_1} - \beta\frac{\Gamma_1^2}{kT} + \left(\frac{8c_{2\infty}}{\pi L_B}\right)^{1/2}\left[cosh\left(\frac{\Phi_s}{2}\right)-1\right] \tag{3.9}$$

where σ_0 is the surface tension of pure water.

All four experimental curves in Fig. 6 are *simultaneously* fitted with the theoretical dependence $\sigma(c_{1\infty},c_{3\infty})$ given by Eqs. (3.5)–(3.9) using Γ_∞, β, K_1 and K_{St} as four adjustable parameters. Their values, corresponding to the best fit, are given in the last row of Table 2.

The parameters of the isotherms for SDS solutions (Table 2) have been determined in Refs. [76,98] and those for CTAB solutions — in Refs. [100,101]. One sees that the area per adsorbed surfactant molecule, $1/\Gamma_\infty$, is the smallest for SDS and the largest for CPC, which reflects the size of the surfactant headgroup. The Stern constant is the smallest for SDS and the largest for CTAB. These results correlate with the fact that the Br^- ions are the least hydrated in comparison with the Cl^- and Na^+ ions [16], and have the greatest affinity to bind to surfaces [102,103].

Table 2
Parameters of the surface tension isotherms for SDS, CTAB, and CPC.

Surfactant	$1/\Gamma_\infty$ (nm^2)	$2\beta\Gamma_\infty/(kT)$	K_1 (1/mM)	K_{St} (1/mM)
SDS [76,98]	0.298	2.7	99.2	6.53×10^{-4}
CTAB [100,101]	0.395	1.0	4.87×10^{3}	7.45×10^{-3}
CPC [Fig. 6]	0.510	0.99	1.38×10^{4}	5.93×10^{-3}

The degree of micelle ionization is $\alpha=(\Gamma_1-\Gamma_2)/\Gamma_1$. The combination of the Stern isotherm, Eq. (3.8), with Eq. (3.6) yields:

$$\alpha=\frac{1}{1+K_{St}\gamma_{\pm}c_{2\infty}\,exp\Phi_s}. \tag{3.10}$$

The values of K_{St} for the investigated surfactants are given in Table 2.

3.3. Conductivity measurements and determination of micelle charge

Our experimental data for the electrolytic conductivity, $\tilde{\kappa}$, of the investigated surfactants in aqueous solutions are given in Fig. 7. The kinks in the conductivity curves agree very well with the known CMC values for these surfactants; see Section 2. In general, our conductivity data are very close to analogous data by other authors for SDS [104–110]; CTAB [83,111–113] and CPC [86–89]. The lower slope of the conductivity curves above the CMC (Fig. 7) is mostly due to the fact that a fraction of the counterions are bound to the micelles. Consequently, the theoretical interpretation of the conductivity curves can give the degree of micelle ionization, α.

The electrolytic conductivity of micellar solutions without added background electrolyte, can be calculated using the following relationship [114,115]:

$$\tilde{\kappa}=\lambda_c^0\alpha(c_s-\mathrm{CMC})+\lambda_{mic}^0c_{mic}-AI^{3/2}+BI^2+\mathrm{const.} \tag{3.11}$$

where λ_c^0 is the limiting molar ionic conductance of the counterions; c_{mic} is the concentration of micelles and λ_{mic}^0 is their molar conductance; I is the ionic strength of the solution; A and B are empirical coefficients in the augmented Kohlrausch law, which take into account the interactions between the ions [116]. The parameters λ_c^0, A and B are tabulated in Ref. [117]. The additive constant in Eq. (3.11) represents the conductivity of some ions, whose concentrations do not change upon increasing the amount of surfactant above the CMC. Such are the surfactant monomers and some background ions as H^+, OH^-, and (probably) HCO_3^-.

The term $\lambda_{mic}^0c_{mic}$ in Eq. (3.11) gives a small contribution to $\tilde{\kappa}$, but for a greater precision we estimate also this term. λ_{mic}^0 can be expressed in the form [115,116]:

$$\lambda_{mic}^0\equiv\alpha N_{agg}\tilde{\lambda}_{mic}^0 \tag{3.12}$$

where by definition

$$\tilde{\lambda}_{mic}^0=\frac{e^2N_A}{3\pi\eta_w d_H} \tag{3.13}$$

characterizes the hydrodynamic mobility of the micelle and does not depend on its charge; N_A is the Avogadro number; η_w is the viscosity of water and, as usual, d_H is the micelle hydrodynamic diameter. The ionic strength and micelle concentration are:

$$I\approx\mathrm{CMC}+\frac{\alpha}{2}(c_s-\mathrm{CMC});\quad c_{mic}=\frac{c_s-\mathrm{CMC}}{N_{agg}}. \tag{3.14}$$

Substituting Eqs. (3.12) and (3.14) in Eq. (3.11), we obtain:

$$\tilde{\kappa}=\alpha\left(\lambda_c^0+\tilde{\lambda}_{mic}^0\right)(c_s-\mathrm{CMC})-AI^{3/2}+BI^2+\mathrm{const.} \tag{3.15}$$

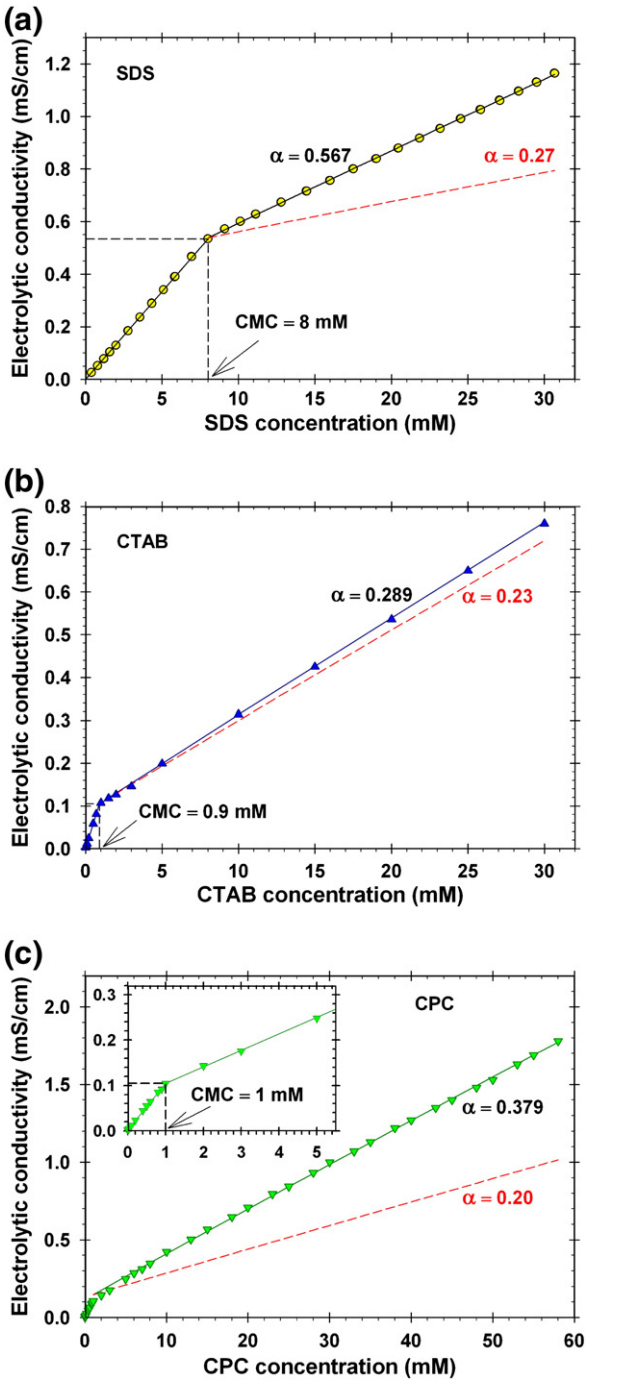

Fig. 7. Plots of electrolytic conductivity, $\tilde{\kappa}$, vs. the surfactant concentration, c_s, for three surfactants: (a) SDS; (b) CTAB and (c) CPC. The solid lines are the best fits by Eq. (3.15); the values of α determined from the fits are shown. The dashed lines show what would be the conductivity if literature values of α are used; details in the text.

Note that Eq. (3.15) contains α, but it does not contain N_{agg}. The values of λ_c^0 for Na^+, Cl^- and Br^- ions are, respectively, 50.10; 76.35 and 78.14 cm^2 S/mol [117,118]. The values of $\tilde{\lambda}_{mic}^0$ estimated from Eq. (3.13) are 4.2 cm^2 S/mol for SDS micelles and 3.4 cm^2 S/mol for CTAB and CPC micelles. These values of $\tilde{\lambda}_{mic}^0$ are much smaller than those of λ_c^0, and the contribution of the micelles to the total conductivity, $\tilde{\kappa}$, is really small. Because A and B are insensitive to the type of electrolyte [114,116], we proceeded as follows. For SDS and CPC (with Cl^- anion), we used their values for NaCl [117]: $A=88.55$ mS cm^{-1} M$^{-3/2}$ and $B=93.61$ mS cm^{-1} M^{-2}. For CTAB (Br^- anion), we used the

respective values for NaBr [117]: $A = 88.20\ \mathrm{mS\ cm^{-1}\ M^{-3/2}}$ and $B = 63.00\ \mathrm{mS\ cm^{-1}\ M^{-2}}$.

To determine α from the conductivity data above the CMC, we used the following iteration procedure.

(1) The input data are the values of λ_c^0, $\tilde{\lambda}_{mic}^0$, A and B; see above.
(2) A tentative value is given to α;
(3) The ionic strength I is calculated from Eq. (3.14).
(4) In view of Eq. (3.15), the data for conductivity above the CMC are plotted as $\tilde{\kappa} + AI^{3/2} - BI^2$ vs. c_s − CMC.
(5) The obtained dependence is fitted with a linear regression, from which slope a new value of α is obtained, and the procedure continues from step (3).

Usually 5 steps are enough to obtain α with a relative error smaller than 10^{-4}.

The fits are shown in Fig. 7 by solid lines. The obtained values of α, their errors and the values of the regression coefficient of the fits are given in Table 3.

The dashed lines in Fig. 7 show what would be the conductivity $\tilde{\kappa}$ if literature data for α are substituted in Eq. (3.15), as follows: for SDS: α = 0.27 determined by electromotive-force measurements [64]; for CTAB: α = 0.23 obtained by several methods [94,119–121]; for CPC: α = 0.20 determined by analysis of SANS data [88]. As seen in Fig. 7, the aforementioned literature data for α lead to predicted conductivity curves that are considerably different from the experimental data, except in the case of CTAB where the difference is not so significant.

It should be noted that the differences in the obtained values of α depend not only on the used experimental method but also on the way of their interpretation. For example, in Refs. [96,97] α = 0.54 was obtained from the slope of the log(CMC) vs. log($c_{2\infty}$) plot for SDS, which is close to the value α = 0.567 in Table 3. However, if the activity coefficient $\gamma_\pm$ is taken into account in the mass-action law and the data from Refs. [96,97] are plotted as log(CMC) vs. log($\gamma_\pm c_{2\infty}$), the result becomes α = 0.313.

It should be also noted that if the values of α from Table 3 are substituted in Eq. (3.3) and the plot in Fig. 5 is redrawn, the result again does not agree with Eq. (3.1). For this reason, a more complex model is needed, which takes into account the energy of interaction between the micelles (see below).

4. Electrostatic potential near a charged spherical particle

4.1. General equations

To calculate α from Eq. (3.10) for nano-sized particles (including micelles), we have to determine the particle dimensionless surface potential, Φ_s. The difficulties with this problem are due to the fact that a dispersion of charged nano-sized particles represents a strongly asymmetric electrolyte that contains small monovalent ions and larger multivalent nanoparticles. Here, we consider and compare three different approaches to the solution of this problem: (i) the conventional Poisson–Boltzmann model; (ii) the jellium approximation [61,62] and (iii) the cell model [122–125]. First, the physical system and the basic equations that are common for the three models are specified.

Table 3
Degree of micelle ionization, α, determined from conductivity (Fig. 7).

Surfactant	α	Error Δα	Regression coefficient
SDS	0.567	±0.001	0.9999
CTAB	0.289	±0.003	0.9995
CPC	0.379	±0.001	0.9998

In general, the particles can be surfactant micelles, solid spheres, liquid drops, or gas bubbles. Let us consider an electrically charged spherical particle of radius a ($a = d_H/2$, where d_H is the hydrodynamic diameter). The particle belongs to a dispersion of similar particles, which can contain also dissolved 1:1 electrolyte. The results could be generalized to the case of m:n electrolyte ($m,n \geq 1$) following the approach in Ref. [99]. The electrostatic potential, ψ, around the considered particle satisfies the Poisson equation:

$$\frac{1}{r^2}\frac{d}{dr}\left(r^2\frac{d\psi}{dr}\right) = -\frac{4\pi}{\varepsilon}\rho_b \quad \text{for} \quad r > a \tag{4.1}$$

where r is the radial coordinate (with origin in the particle center) and ρ_b is the bulk charge density; as usual, ε is the dielectric constant of the continuous phase, in our case water. The electric field inside the spherical particle is considered to be zero, so that the standard electrostatic boundary condition at the particle surface reads [126–128]:

$$\frac{d\psi}{dr} = -\frac{4\pi}{\varepsilon}\rho_s \quad \text{at} \quad r = a \tag{4.2}$$

where ρ_s is the surface charge density. In addition, we have

$$\rho_s = \frac{Ze}{4\pi a^2} \quad \text{and} \quad \Phi \equiv \frac{ze\psi}{kT} \tag{4.3}$$

where Z is the effective particle (micelle) charge in units of the elementary charge e; in the case of micelles, $Z = \alpha N_{agg}$; Φ is the dimensionless electrostatic potential; $z = +1$ or -1, respectively, for a positively or negatively charged particle. In view of Eq. (4.3) and the definition of the Bjerrum length in Eq. (3.3), Eq. (4.2) acquires the form:

$$\frac{d\Phi}{dr} = -\frac{ZL_B}{a^2} \quad \text{at} \quad r = a. \tag{4.4}$$

In the case of ionic-surfactant micelles, we have three types of small ions: (i) surfactant monomers of concentration c_1; (ii) counterions of concentration c_2 and (iii) coions of the added electrolyte of concentration c_3. Here and hereafter, we assume that the counterions dissociated from the micelles (particles) and the counterions from the added electrolyte are of the same kind (e.g. Na^+ ions in the case of SDS, or Cl^- ions in the case of CPC). In the electric field of the considered micelle (particle), the small ions are assumed to obey the Boltzmann distribution:

$$c_1 = c_{1\infty}\, exp(-\Phi), \quad c_2 = c_{2\infty}\, exp\Phi, \quad c_3 = c_{3\infty}\, exp(-\Phi) \tag{4.5}$$

where $c_{i\infty}$ ($i = 1, 2, 3$) are the mean concentrations of the respective ions far from the charged micelle (particle). Because counterions are dissociated from both the particles (micelles) and the dissolved electrolyte, the electroneutrality condition reads:

$$c_{2\infty} = Zc_{p\infty} + c_{1\infty} + c_{3\infty} \tag{4.6}$$

where, $c_{p\infty}$ is the mean concentration of particles far from the considered charged particle. In the cases of particles and micelles, we have, respectively:

$$c_{1\infty} = 0 \quad \text{(particles)} \tag{4.7}$$

$$c_{1\infty} = \mathrm{CMC}, \quad Zc_{p\infty} = \alpha(c_s - \mathrm{CMC}), \quad Z = \alpha N_{agg} \quad \text{(micelles)}. \tag{4.8}$$

4.2. Poisson–Boltzmann (PB) model

In this model, the particles (micelles) obey the Boltzmann distribution [16,129]:

$$c_p = c_{p\infty}\, exp(-Z\Phi) \tag{4.9}$$

just as the small ions; see Eq. (4.5). With the help of Eqs. (4.3), (4.5), (4.6) and (4.9), Eq. (4.1) can be represented in the form:

$$\frac{1}{r^2}\frac{d}{dr}\left(r^2\frac{d\Phi}{dr}\right) = 4\pi L_B\left[2(c_{1\infty}+c_{3\infty})\, sinh(\Phi) + Zc_{p\infty}\left(e^{\Phi}-e^{-Z\Phi}\right)\right] \tag{4.10}$$

for $r>a$. Eq. (4.10) represents the Poisson–Boltzmann equation for the considered asymmetric system. In the case of small electrostatic potential, $Z\Phi \ll 1$, Eq. (4.10) reduces to:

$$\frac{1}{r^2}\frac{d}{dr}\left(r^2\frac{d\Phi}{dr}\right) = \kappa_{PB}^2\Phi \quad \text{for } r>a \tag{4.11}$$

where the Debye parameter for the PB model is defined as follows:

$$\kappa_{PB}^2 \equiv 8\pi L_B\left[c_{1\infty}+c_{3\infty}+\frac{1}{2}\left(Z+Z^2\right)c_{p\infty}\right]. \tag{4.12}$$

The electrostatic potential vanishes at long distances from the particle:

$$\Phi\to 0 \quad \text{for } r\to\infty. \tag{4.13}$$

Thus the PB boundary problem consists of Eq. (4.10) and two boundary conditions, Eqs. (4.4) and (4.13).

In the case of a strongly asymmetric electrolyte, the considered version of Poisson–Boltzmann model is not completely adequate because it treats both the small ions and the larger particles (micelles) as *point* ions of different charges. However, in reality the size of the particles is much greater than that of the conventional ions, and the particles repel each other much stronger than two similar small ions. For this reason, other models have been proposed to account more adequately for the asymmetry of the system; see below.

4.3. Jellium approximation (JA) model

In the jellium approximation [61,62], instead of the Boltzmann distribution, Eq. (4.9), we have a uniform distribution of particles (micelles):

$$c_p = c_{p\infty} = \text{const.} \tag{4.14}$$

Physically, Eq. (4.14) means that the interparticle electrostatic repulsion is much stronger than the effect of the double-layer electric field. In view of Eq. (4.14), the Poisson–Boltzmann equation in the jellium approximation acquires the form:

$$\frac{1}{r^2}\frac{d}{dr}\left(r^2\frac{d\Phi}{dr}\right) = 4\pi L_B\left[2(c_{1\infty}+c_{3\infty})\, sinh(\Phi) + Zc_{p\infty}\left(e^{\Phi}-1\right)\right] \tag{4.15}$$

for $r>a$. For small values of the electrostatic potential, $\Phi \ll 1$, Eq. (4.15) can be linearized:

$$\frac{1}{r^2}\frac{d}{dr}\left(r^2\frac{d\Phi}{dr}\right) = \kappa^2\Phi \quad \text{for } r>a \tag{4.16}$$

where the screening parameter κ is defined as follows:

$$\kappa^2 \equiv 8\pi L_B\left(c_{1\infty}+c_{3\infty}+\frac{Z}{2}c_{p\infty}\right). \tag{4.17}$$

Note that Eq. (4.17) is identical to Eq. (3.3), which has been already used.

The comparison of Eqs. (4.12) and (4.17) shows that $\kappa_{PB}>\kappa$. Physically, this difference originates from the fact that in the PB model the macro-ions (particles or micelles) also take part in the Debye screening of the electric field, unlike the case of jellium approximation. The JA boundary problem consists of Eq. (4.15) and two boundary conditions, Eqs. (4.4) and (4.13).

The JA model was first introduced in Refs. [61,62] and further applied to study phase diagrams of charged colloids [130,131]; structuring and short time dynamics in suspensions of charged particles [132,133]; contributions of macroion correlations and volume exclusion effects to the osmotic pressure [134–137], as well as the reappearance of structures in colloidal suspensions [138–140].

4.4. Cell model (CM)

The cell model was originally proposed to describe the osmotic pressure and bulk modulus of colloidal crystals [122–125]. The particles (micelles) are assumed to be fixed in the nodes of a regular lattice. The small ions are distributed in the electric field of the fixed particles. The Poisson–Boltzmann equation for the mean electrostatic potential, Φ, is written for a separate Wigner–Seitz cell of the lattice, which is usually approximated with a spherical cell of radius b:

$$\frac{1}{r^2}\frac{d}{dr}\left(r^2\frac{d\Phi}{dr}\right) = 4\pi L_B\left[2(c_{1\infty}+c_{3\infty})\, sinh(\Phi) + Zc_{p\infty}e^{\Phi}\right] \tag{4.18}$$

for $a<r<b$. Because the potential Φ should be minimal in the middle between two particles, its derivative is set to zero at the outer boundary of the cell:

$$\frac{d\Phi}{dr} = 0 \quad \text{for} \quad r=b. \tag{4.19}$$

The CM boundary problem consists of Eq. (4.18) and two boundary conditions, Eqs. (4.4) and (4.19). In this model, each cell is electroneutral, which guarantees the electroneutrality of the whole system. The outer radius of the cell, b, is determined from the condition of the volume of the cell to be equal to the volume per particle (micelle) in the solution, viz. $(4/3)\pi b^3 = 1/c_{p\infty}$.

The cell model has found applications in the theory of growth of charged micelles [141]; for calculation of the effective charge and charge renormalization [142–149]; for measurements and dynamic tests of interaction potentials of charge-stabilized colloids [150,151]; for calculation of the force between macroions [152–155]; for studies on stability and phase behavior of charged colloids [156–161]; and for complex colloid systems such as lamellar colloids, swollen clays, and microgels [162–164]. Klein et al. [165] generalized the cell model by including the Stern isotherm of charge regulation.

The limits of validity of the Poisson–Boltzmann model, jellium approximation, and cell model are discussed in Refs. [166,167]. Their predictions regarding $\Phi(r)$ and $\alpha(c_s)$ are compared in the next section.

4.5. Numerical results: potential and degree of micelle ionization

To determine the dependence $\Phi(r)$ of the electrostatic potential on the distance from the center of the particle (micelle), we solved the *nonlinear* Poisson–Boltzmann equation numerically, along with the respective boundary conditions (see above). Thus, for the PB, JA and cell models we solved, respectively, Eqs. (4.10), (4.15) and (4.18).

An additional difficulty is related to the fact that the parameter α (degree of micelle ionization) appears in both the differential equation and boundary condition, but to determine α we have to substitute the calculated surface potential Φ_s into Eq. (3.10). For this

reason, we applied iterations, using the values of α in Table 3 as a zero-order approximation. The computational procedure is described in Appendix A. The values of α shown in Figs. 8–10 represent results of the iteration procedure.

The values of the input parameters are listed in Table 4. The micelle radius is determined as $a = d_H/2$, where d_H is given by Eqs. (2.1)–(2.3). The micelle aggregation number, N_{agg}, taken from different references, is given in the last column of Table 4.

Fig. 8 compares the electrostatic potentials predicted (i) by the approximate *linearized* models, based on Eqs. (4.11) and (4.16), and denoted LPB and LJA, and (ii) by the exact models based on the respective nonlinear differential equations, Eqs. (4.10) and (4.15) for the PB and JA models. The principles of the computational procedure are described in Appendix A. In the considered example, the system is a 30 mM solution of SDS with 0 and 100 mM NaCl. Under these conditions, the boundary problem is solved for each model; the potential at the micelle surface, Φ_s, is determined and substituted in Eq. (3.10) to calculate the degree of ionization, α. The values of α thus obtained are different for the different models and are given in Fig. 8. The values of α in Fig. 8a (no added salt) for the two nonlinear models (0.578 for PB and 0.569 for JA) are very close to the value $\alpha = 0.567$ independently determined from the data for conductivity (Table 3). The presence of 100 mM NaCl leads to a decrease in the ionization degree with $\Delta\alpha \approx 0.04$ for both PB and JA (Fig. 8b), which means that more Na^+ counterions are bound to the micelle $-SO_4^-$ groups at a higher NaCl concentration. Note that the value of the binding constant K_{St} for SDS in Table 2 is essentially used in these calculations.

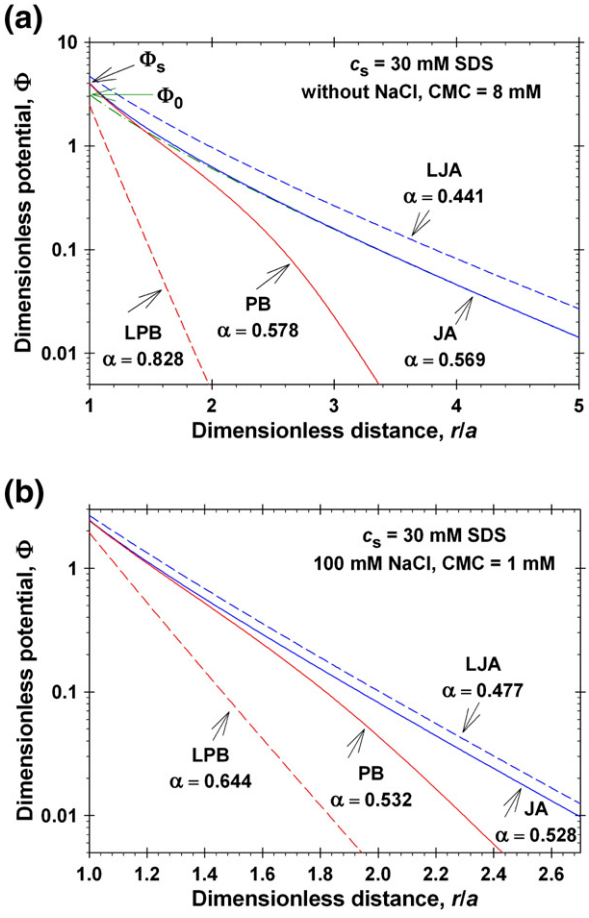

Fig. 8. Plots of the calculated dimensionless surface potential, Φ, vs. the distance, r from a spherical micelle of radius $a = 2.3$ nm in a solution of 30 mM SDS. The values of the ionization degree, α, calculated for this SDS concentration using K_{St} (charge regulation) are shown for each curve. The curves correspond to the Poisson–Boltzmann (PB) and jellium approximation (JA) models, and to their linearized versions, LPB and LJA. (a) No added salt; Φ_s is the JA surface potential; Φ_0 is the renormalized surface potential, i.e. the coefficient in the asymptotic Eq. (4.20), which is plotted by dash–dot line. (b) With 100 mM added NaCl.

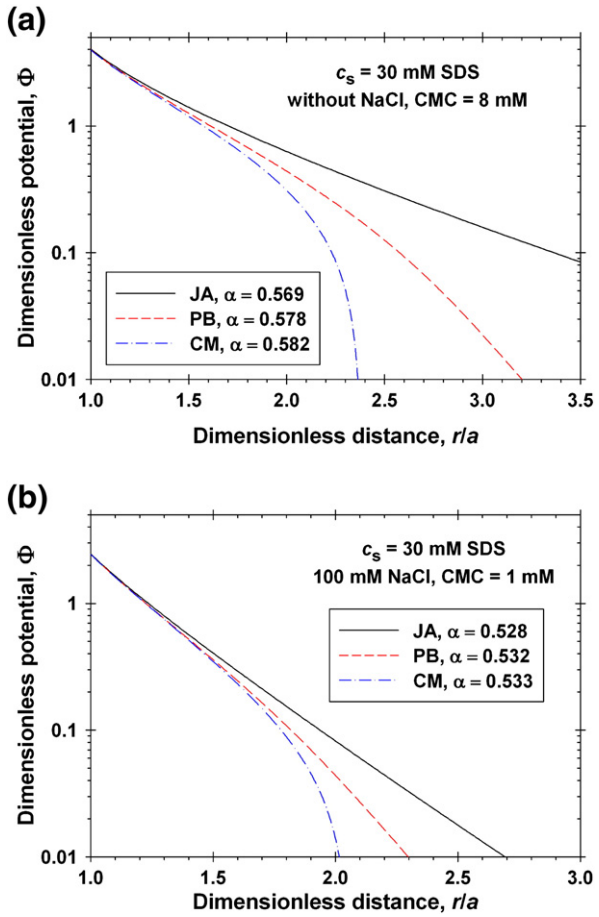

Fig. 9. Comparison of the three models, PB, JA and CM, with respect to their predictions for the dimensionless electrostatic potential, $\Phi(r)$. The systems and parameter values are as in Fig. 8. The values of the ionization degree, α, calculated for $c_s = 30$ mM SDS using K_{St} (charge regulation) are shown for each curve. (a) No added salt. (b) With 100 mM added NaCl.

The $\Phi(r)$-curves predicted by the linearized models, LPB and LJA, considerably differ from the exact dependences of the PB and JA models (note that the vertical scale in Fig. 8 is logarithmic). The difference is greater for the PB model and in the absence of NaCl. These results demonstrate that the problem is essentially nonlinear, so that a numerical solution of the exact nonlinear boundary problem cannot be avoided if the aim is to obtain quantitatively correct results.

However, it should be noted that at sufficiently large distances from the particle the potential Φ always becomes low, so that the differential equation, Eq. (4.10) or (4.15), can be linearized in that region. In other words, the *asymptotic behavior* of the dependence $\Phi(r)$ is described by the solution of the linearized problem:

$$\Phi(r) \approx \Phi_0 \frac{a}{r} \exp[-\kappa(r-a)] \text{ for } \Phi << 1. \quad (4.20)$$

where κ is given by Eq. (4.17) for the JA model, and $\kappa = \kappa_{PB}$ for the PB model; see Eq. (4.12); Φ_0 is the limiting value predicted by Eq. (4.20) upon being extrapolated to $r/a \to 1$; see the dash–dotted line in Fig. 8a. Φ_0 is sometimes called the *renormalized* surface potential. It is a parameter of the asymptotic Eq. (4.20) that, in general, is different from the *true* surface potential Φ_s (Fig. 8a). In Fig. 8a, $\Phi_0 < \Phi_s$ for the JA model. Similar extrapolation for the PB model would lead to $\Phi_0 > \Phi_s$.

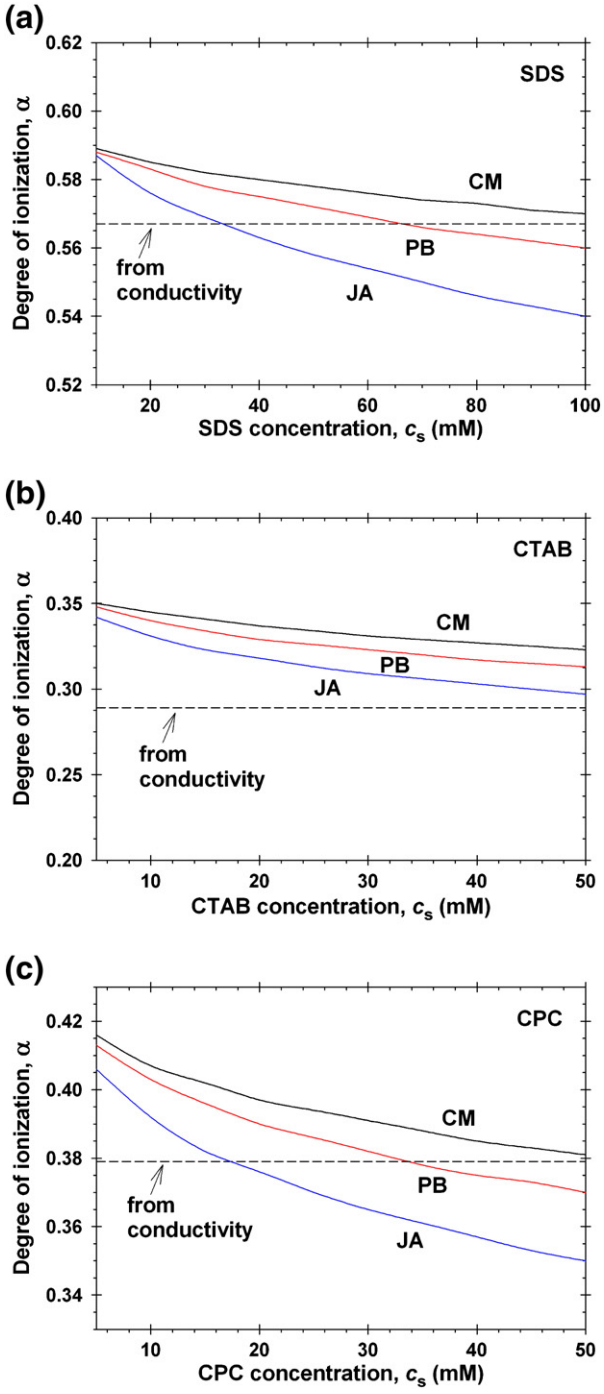

Fig. 10. Calculated degree of micelle ionization, α, vs. the surfactant concentration, c_s: predictions of the three models: PB, JA and CM. The dashed lines denote the mean value of α determined from the conductivity data (Fig. 7). (a) SDS; (b) CTAB, and (c) CPC.

Another feature of the investigated problem is that the values of the surface potential Φ_s calculated by using the different *nonlinear* models (PB and JA) are practically the same; see Fig. 8. This is seen also in Fig. 9, where the three nonlinear models, PB, JA and CM, are compared. In fact, there are some differences that are reflected by the values of α for the different models, see Eq. (3.10), however these differences are so small that they are invisible in Figs. 8 and 9. The reason for this behavior is that the surface potential is not low so that the counterion term $\propto \sinh(\Phi)$, which is the same in Eqs. (4.10), (4.15) and (4.18), determines $\Phi(r)$ near the surface. On the other hand, the linearized models (Fig. 8) give different Φ_s, because the linearization $\sinh(\Phi)\approx\Phi$ is incorrect close to the micelle surface.

Fig. 9 shows that at greater distances the three models give different predictions. In the range of distances shown in Fig. 9, JA predicts the greatest $\Phi(r)$; CM predicts the smallest $\Phi(r)$, whereas the prediction of the PB model is in the middle. At longer distances, PB predicts the fastest decay of $\Phi(r)$ [we recall that $\kappa_{PB}>\kappa$ and the asymptotics is given by Eq. (4.20)], whereas in CM $\Phi(r)$ is defined only inside the cell, $a\le r\le b$. The long-range asymptotics of $\Phi(r)$ is important, because it determines the interaction between the micelles (particles) in the thin films, and the height of the stratification steps, Δh; see Section 6.2.

Fig. 10 shows the dependence of the degree of micelle ionization, α, on the surfactant concentration, c_s. Because c_s affects the concentration of the ionic species and the Debye screening parameter, κ, it influences also the surface potential Φ_s, and the degree of ionization, α, see Eq. (3.10). As seen in Fig. 10, α decreases with the rise of c_s (due to increased counterion binding), but the variations in α are not too large. For the three investigated surfactants, the JA model gives the smallest α, whereas CM yields the largest α (Fig. 10). The value of α strongly depends on the Stern binding parameter K_{St}. The reliable determination of this parameter is crucial for the quantitative theory considered in the present article. A very important result is that all three models give α close to that independently determined from conductivity (the dashed line in Fig. 10; see also Table 3), the latter being an average value for the whole concentration region above the CMC (see Fig. 7). This agreement supports the adequacy of the approach based on the charge-regulation concept, expressed by Eq. (3.10). Below, we will use the calculated α-vs.-c_s dependencies, like those shown in Fig. 10, to quantitatively interpret the experimental $h_0(c_s)$ and $\Delta h(c_s)$ curves; see Figs. 4 and 5.

5. Disjoining pressure and thickness of the final stable film

The equilibrium thickness, h_0, of the thinnest final stable film can be found by using the condition for mechanical equilibrium of the film [170]:

$$\Pi(h_0) = P_c \tag{5.1}$$

where $\Pi(h)$ is the theoretical dependence of disjoining pressure Π on the film thickness h, and P_c is the experimental capillary pressure. Eq. (5.1) expresses the fact that the applied sucking pressure, P_c, that presses the two film surfaces against each other is counterbalanced by the repulsion between the film surfaces, expressed by the disjoining pressure Π. The value of P_c can be estimated from the capillary pressure of the meniscus in the SE cell [4]: $P_c\approx 2\sigma/R_c$, where $R_c = 1.5$ mm is the inner radius of the used SE cell, and σ is the surface tension of the surfactant solution at the CMC; see Table 5.

Table 4
Parameters used to calculate the curves in Figs. 8–10.

Surfactant	Micelle radius, a (nm)	Aggregation number, N_{agg}	Reference for N_{agg}
SDS	2.27	67	[168]
CTAB	2.87	95	[169]
CPC	2.92	78[a]	[87]

[a] From the comparison of the JA model with conductivity data at 20 mM CPC, Fig. 10c.

Table 5
Solution's surface tension at the CMC, σ, and capillary pressure P_c.

Surfactant	σ (mN/m)	P_c (Pa)
SDS	39	52
CTAB	37	49
CPC	42	56

In the considered case ($h = h_0$), the disjoining pressure is a superposition of van der Waals attraction, Π_{vw}, and electrostatic repulsions, Π_{el} [171,172]

$$\Pi(h) = \Pi_{vw}(h) + \Pi_{el}(h). \tag{5.2}$$

The depletion interaction due to the micelles in the Plateau border is taken into account in Π_{el} (see below). The van der Waals component can be accurately calculated from the equation

$$\Pi_{vw}(h) = -\frac{A(h)}{6\pi h^3}. \tag{5.3}$$

The Hamaker parameter $A(h)$ depends on the film thickness, h, because of the electromagnetic retardation effect, as follows [173]:

$$A = 2\kappa h A_0\, exp(-2\kappa h) + \frac{3h_P\nu_e}{4\pi}\frac{\left(n_w^2-1\right)^2}{\left(n_w^2+1\right)^{3/2}}\int_0^\infty \frac{\left(1+2\tilde{h}z\right)}{\left(1+2z^2\right)^2} exp\left(-2\tilde{h}z\right)dz. \tag{5.4}$$

Here: $h_P = 6.63\times10^{-34}$ J·s is the Plank constant; $\nu_e = 3\times10^{15}$ Hz is the main electronic adsorption frequency; $n_w \approx 1.333$ is the refractive indexes of water; $c_0 = 3.0\times10^8$ m/s is the speed of light in vacuum; $\tilde{h} \equiv 2\pi\nu_e h n_w \left(n_w^2+1\right)^{1/2}/c_0$ is a dimensionless thickness; z is an integration variable; and A_0 is the "zero-frequency" contribution to $A(h)$. In our case, the contribution of the term with A_0 is negligible because the orientation and induction interactions are screened by the electrolyte [16], which is taken into account by the factor exp $(-2\kappa h)$ in Eq. (5.4).

The electrostatic component of disjoining pressure equals the difference between the osmotic pressures in the midplane of the film and in the bulk solution [16,127,128,174]:

$$\Pi_{el} = (P_{osm})_{midplane} - (P_{osm})_{bulk}. \tag{5.5}$$

The bulk osmotic pressure can be estimated from the expression:

$$(P_{osm})_{bulk} = kT\left[2(c_{1\infty} + c_{3\infty}) + (Z+1)c_{p\infty}\right]. \tag{5.6}$$

The first term in the brackets in Eq. (5.6) expresses the contributions from the surfactant monomers ($c_{1\infty}$), coions from the added electrolyte ($c_{3\infty}$) and their counterions (the multiplier 2). The second term in the brackets is the contribution of the micelles/particles ($c_{p\infty}$) and of the counterions dissociated from them ($Zc_{p\infty}$).

We consider a liquid film of electrically charged surfaces that contains micelles (or particles), which have the same sign of the charge as the film surfaces. Such are the foam films from micellar solutions of an ionic surfactant that are experimentally investigated in Section 3; see Figs. 1–3. There are two possible models for the final equilibrium state that is reached after the thinning of such a film. Model A: micelles/particles are not present inside the film (Fig. 11a). Indeed, most frequently, it is intuitively expected that the final state of a stratifying film should not contain micelles/particles [5,16]. Model B: the micelles/particles are present inside the final film (Fig. 11b). Model B is counterintuitive, but it should be noted that the experimental final thickness, h_0, is several times greater that the micelle diameter, d_H; compare Eqs. (2.1)–(2.3) with Fig. 4. Hence, in principle the micelles could penetrate between the surfaces of a film of thickness h_0. However, the film surfaces strongly repel the similarly charged micelles, so that their concentration inside the film (if different from zero) should be rather low.

We carried out calculations using the two versions of the model (Fig. 11a and b). The results show that the predictions of the model corresponding to Fig. 11a do not agree with the experimental h_0-vs.-c_s data. In contrast, the model from Fig. 11b agrees excellently with

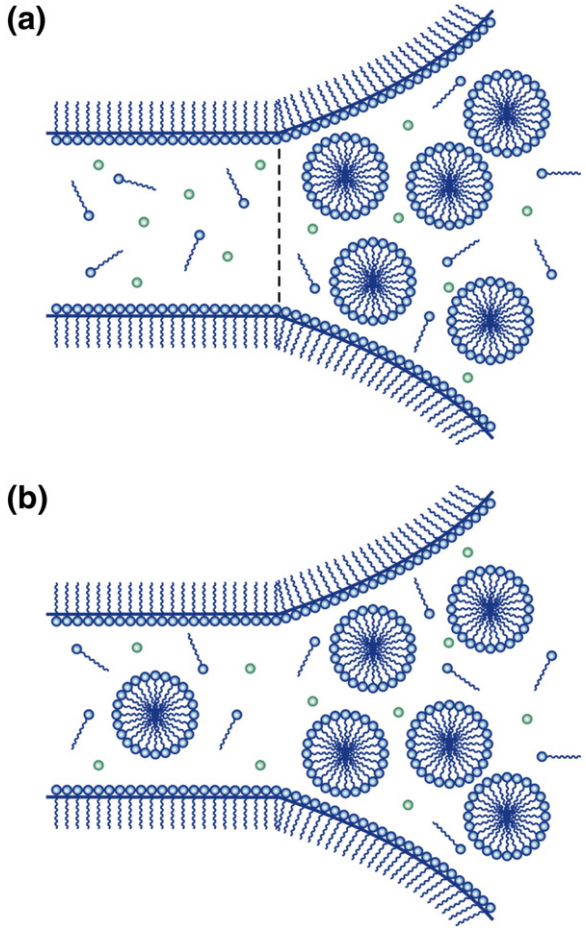

Fig. 11. The final state of the film with thickness h_0: Sketches of the two possible models. (a) Micelles do not penetrate in the film. (b) Micelles are present in the film at a concentration, which is much lower than that in the bulk solution.

these data, without adjusting any parameters. For this reason, here we present only the latter model, which leads to the following expression for the osmotic pressure in the film's midplane:

$$(P_{osm})_{midplane} = kT\left[(c_{1\infty}+c_{3\infty})\left(e^{\Phi_m}+e^{-\Phi_m}\right) + Zc_{p\infty}e^{\Phi_m} + c_{p\infty}e^{-Z\Phi_m}\right]. \tag{5.7}$$

Correspondingly, the Poisson–Boltzmann equation can be presented in the form:

$$\frac{d^2\Phi}{dx^2} = 4\pi L_B\left[2(c_{1\infty}+c_{3\infty})\, sinh\Phi + Zc_{p\infty}\left(e^{\Phi}-e^{-Z\Phi}\right)\right]. \tag{5.8}$$

Here, the x-axis is perpendicular to the film surfaces and $x = 0$ corresponds to the midplane of the film. To take a first integral, we multiply Eq. (5.8) by $2d\Phi/dx$ and integrate from $x = 0$ to an arbitrary x:

$$\left(\frac{d\Phi}{dx}\right)^2 = 8\pi L_B F(\Phi,\Phi_m) \tag{5.9}$$

$$F(\Phi,\Phi_m) \equiv 2(c_{1\infty}+c_{3\infty})(\,cosh\Phi - cosh\Phi_m) + Zc_{p\infty}(e^{\Phi}-e^{\Phi_m}) + c_{p\infty}(e^{-Z\Phi}-e^{-Z\Phi_m}). \tag{5.10}$$

In Eq. (5.9), the boundary condition $(d\Phi/dx)_{x=0} = 0$ has been taken into account. Furthermore, we take a square root of Eq. (5.9)

and integrate from the midplane $x=0$ to the film surface at $x=\tilde{h}/2$:

$$(2\pi L_B)^{1/2}\tilde{h} = \int_{\Phi_m}^{\Phi_s} [F(\Phi,\Phi_m)]^{-1/2} d\Phi \tag{5.11}$$

where $\tilde{h} = h - h_a$ is the thickness of the aqueous core of the film; h is the full film thickness, including the two surfactant adsorption layers, each of them of thickness $h_a/2$; see Fig. 11; Φ_s is the electrostatic potential at the film surface.

To calculate the electrostatic potential at the film surfaces, Φ_s, we used the boundary condition that relates the derivative of surface potential to the surface charge density [16,127,128]:

$$\left.\frac{d\Phi}{dx}\right|_{x=\tilde{h}/2} = 4\pi L_B(\Gamma_1 - \Gamma_2) \tag{5.12}$$

where Γ_1 and Γ_2 are the adsorptions of surfactant and counterions at the film surface. Substituting $d\Phi/dx$ from Eq. (5.9) into the left-hand side of Eq. (5.12), we obtain:

$$\Gamma_1 - \Gamma_2 = \left[\frac{1}{2\pi L_B} F(\Phi_s,\Phi_m)\right]^{1/2}. \tag{5.13}$$

Eq. (5.13) represents a generalization of the Gouy equation, Eq. (3.7).

Numerically, it is convenient to seek the dependence $\Pi_{el}(h)$ in parametric form, viz. $\Pi_{el}=\Pi_{el}(\Phi_m)$ and $h=h(\Phi_m)$. For a given Φ_m, Eqs. (3.5), (3.6), (3.8) and (5.13) form a system determining a_{1s}, a_{2s}, Γ_1, Γ_2 and Φ_s. We are using the same computational procedure as in Section 3.2, with the only difference that Eq. (3.7) is replaced by Eq. (5.13). The obtained value of Φ_s is substituted in Eq. (5.11) and $h(\Phi_m)$ is determined by numerical calculation of the integral. In addition, $\Pi_{el}(\Phi_m)$ is calculated from Eqs. (5.5)–(5.7) for the same Φ_m. Thus, by varying Φ_m, we obtain the whole dependence $\Pi_{el}(h)$.

This procedure generalizes the known DLVO procedure [127,128,171] in two respects: (i) presence of micelles (particles) in the bulk of solution is taken into account, and (ii) the more general boundary condition of charge regulation is applied.

In our calculations, we used the following parameter values: K_{St} was taken from Table 1; $Z=\alpha N_{agg}$, where N_{agg} is given in Table 4; α was calculated by the JA model as in Fig. 10; P_c is from Table 5; $c_{1\infty}=$ CMC; $c_{3\infty}=0$ (no added salt); $c_{2\infty}$ is given by Eq. (4.6) and $c_{p\infty}$ — by Eq. (4.8).

As an illustration, Fig. 12a shows the disjoining-pressure isotherms, $\Pi(h)=\Pi_{vw}+\Pi_{el}$, for two SDS concentrations, $c_s=20$ and 50 mM. The isotherm at $c_s=50$ mM corresponds to smaller film thicknesses because of the higher ionic strength that suppresses the electrostatic repulsion. The intersection point of each isotherm with the horizontal line $\Pi=P_c$ determines the value of h_0 for the respective c_s. The results for h_0 vs. c_s thus obtained are shown with the solid lines in Fig. 12b, where the points represent the respective experimental data from Fig. 4. One sees that the theoretical curves excellently agree with the experimental data; no adjustable parameters have been used.

If $\Phi_m=0.1$ and $Z=30$, then $\exp(-Z\Phi_m)\approx 0.05$, i.e. the concentration of micelles in the film of thickness h_0 is only 5% of the bulk micelle concentration $c_{p\infty}$; see the last term in Eq. (5.7). In other words, in its final state of thickness h_0, the film contains separate micelles (Fig. 11b), which take part in the balance of osmotic pressures between the film interior and the bulk solution. In contrast, the film of thickness h_1 (Fig. 1) contains a real monolayer of micelles, whose counterion atmospheres are pressed against each other (see below).

It should be noted that the model of a film where micelles or other charged particles do not penetrate (the model A in Fig. 11a) can be also realized, although at other experimental conditions. For example, if a sufficient amount of electrolyte is added to the solution, the obtained films would become so thin that micelles would be unable to penetrate them.

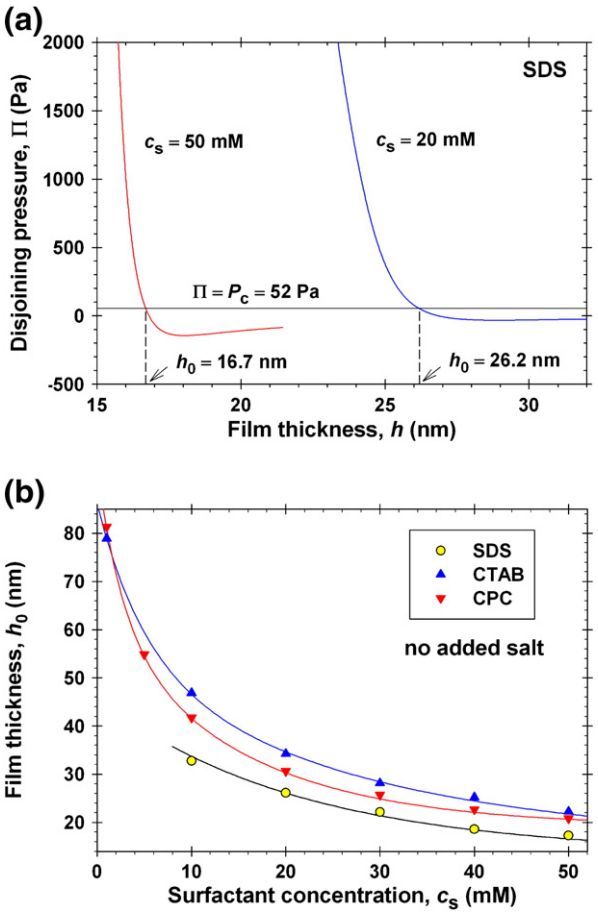

Fig. 12. (a) Disjoining pressure, $\Pi=\Pi_{el}+\Pi_{vw}$, vs. the film thickness, h, calculated for two surfactant concentrations, $c_s=20$ and 50 mM SDS, as explained in the text. The condition $\Pi(h_0)=P_c$ determines the theoretical equilibrium thickness h_0 of the final stable film. (b) Plots of h_0 vs. c_s: the points are data from Fig. 4; the solid lines are predicted by the theory without using any adjustable parameters.

If the model A is applied to the considered case of foam films from micellar solutions of ionic surfactants without added salt, then the calculated Π-vs.-h curves are shifted downwards with respect to the curves in Fig. 12a, which have been obtained by means of the model B. This is due to the sucking osmotic pressure of the micelles (and their dissociated counterions) in the Plateau border around a film that does not contain micelles (model A).

6. Interpretation of the step height, Δh

6.1. Effective diameter of a charged particle (micelle)

In the case of nonionic surfactant, the micelles can be successfully modeled as hard spheres. Then, the height of the step, Δh is very close to the hard-sphere diameter [19,38,59,60]. As discussed in Section 3, in the case of electrically charged particles an effective diameter, d_{eff}, can be introduced. We compared the consequences of different possible definitions of d_{eff} with the experimental data in Fig. 4, and established that the only definition, which leads to agreement between theory and experiment, is given by the expression:

$$\frac{2}{3}\pi(d_{eff})^3 = \frac{1}{2}\int_0^\infty \left[1 - exp\left(-\frac{u(r)}{kT}\right)\right] 4\pi r^2 dr \tag{6.1}$$

where $u(r)$ is the energy of interaction between two charged particles. From a statistical viewpoint, the right-hand side of Eq. (6.1) equals the second virial coefficient, B_2, in the expansion of pressure in powers of the density [175]. As is known, B_2 accounts for the two-particle interactions. In the two-dimensional case, a similar expression was proposed by Adamczyk and Weronski [176], which was successfully applied to interpret data for the adsorption of charged particles at solid surfaces [177–179].

To test Eq. (6.1), let us first consider the case of hard spheres:

$$u(r) = \begin{cases} \infty & \text{for } r < 2a \\ 0 & \text{for } r > 2a \end{cases}. \tag{6.2}$$

Substituting Eq. (6.2) in Eq. (6.1), we obtain that the effective diameter is equal to the hard-sphere diameter, $d_{\text{eff}} = 2a$, as it should be expected. In the case of charged particles, instead of Eq. (6.2), we have:

$$u(r) = \begin{cases} \infty & \text{for } r < 2a \\ u_{\text{el}}(r) & \text{for } r > 2a \end{cases}. \tag{6.3}$$

Here, $u_{\text{el}}(r)$ is the energy of electrostatic repulsion between two particles. The substitution of Eq. (6.3) in Eq. (6.1) yields:

$$d_{\text{eff}} = 2a\left\{1 + \frac{3}{(2a)^3}\int_{2a}^{\infty}\left[1 - exp\left(-\frac{u_{\text{el}}(r)}{kT}\right)\right]r^2 dr\right\}^{1/3}. \tag{6.4}$$

For $u_{\text{el}} \equiv 0$, Eq. (6.4) gives again $d_{\text{eff}} = 2a$, as it should be.

6.2. Energy approach to the interpretation of Δh

To calculate d_{eff} from Eq. (6.4), we need an expression for $u_{\text{el}}(r)$. The force of interaction between two charged particles immersed in electrolyte solution can be estimated from the expression (see Appendix B for details):

$$F_x = \frac{kT}{8\pi L_{\text{B}}}\int_{-\infty}^{\infty}\int_{-\infty}^{\infty}(\Phi_1 + \Phi_2)\frac{\partial^2(\Phi_1 + \Phi_2)}{\partial x^2}dydz \quad \text{at} \quad x = 0. \tag{6.5}$$

In Eq. (6.5), the integration is carried out in the midplane between two particles; see Fig. 13 for the notations. There, the electrostatic potential has been assumed to be low, $\Phi|_{x=0} \ll 1$, so that the superposition approximation can be applied, $\Phi = \Phi_1 + \Phi_2$ at $x = 0$, where Φ_1 and Φ_2 are the dimensionless electrostatic potentials created at a distance $L/2$ by each of the two particles in isolation. Furthermore, for a low potential in the midplane, Φ_1 and Φ_2 can be expressed by the asymptotic Eq. (4.20). Then, the integrals in Eq. (6.5) can be solved analytically, and we obtain the following expression for the electrostatic force:

$$F_x = \frac{kTa^2\Phi_0^2}{L_{\text{B}}L^2}(1 + \kappa L)\, exp[-\kappa(L - 2a)] \tag{6.6}$$

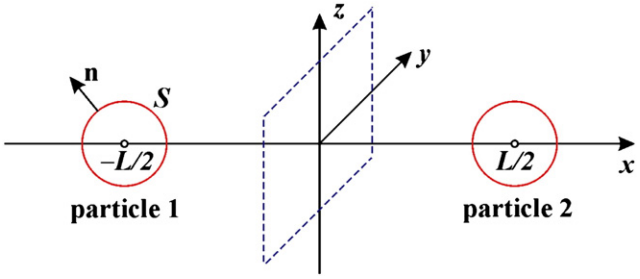

Fig. 13. Sketch of two identical particles separated at a center-to-center distance L. The x-axis of the Cartesian coordinate system passes through the particles' centers, whereas the midplane coincides with the yz-plane.

where L is the center-to-center distance between the two particles; F_x is the force exerted on particle 2, which is acting along the positive direction of the x-axis (see Fig. 13); it has been assumed that the two particles are identical. Integrating Eq. (6.6) with respect to L, we obtain an asymptotic expression for the interaction energy u_{el}:

$$\frac{u_{\text{el}}(L)}{kT} = \frac{a^2}{L_{\text{B}}L}\Phi_0^2\, exp[-\kappa(L - 2a)]. \tag{6.7}$$

As demonstrated in Appendix B, Eq. (6.7) holds for both the PB and JA models, for which κ is defined by Eqs. (4.12) and (4.17), respectively. We recall that Φ_0 in Eq. (6.7) is the renormalized surface potential that enters Eq. (4.20). Alternatively, Eq. (6.7) can be expressed in terms of the renormalized particle charge, Z_0, as follows. First, we formally substitute $\Phi(r)$ from Eq. (4.20) into the boundary condition, Eq. (4.4) with $Z \equiv Z_0$, which yields $\Phi_0 = Z_0 L_{\text{B}}/[(1 + \kappa a)a]$. Next, we substitute the latter expression for Φ_0 in Eq. (6.7) and use the definition for L_{B} in Eq. (3.3); the result reads:

$$u_{\text{el}}(L) = \frac{Z_0^2 e^2}{(1 + \kappa a)^2}\frac{exp[-\kappa(L - 2a)]}{\varepsilon L}. \tag{6.8}$$

Eq. (6.8) is widely used; see e.g. Refs. [173,178,179]. However, it should be noted that it is an asymptotic equation that is valid in the case of low potential in the midplane, $\Phi|_{x=0} \ll 1$. Moreover, Z_0 is the renormalized, rather than the true surface charge.

Setting $r = L/2$ in Eq. (4.20), we obtain:

$$\Phi(L/2) = \Phi_0\frac{2a}{L}\, exp[-\kappa(L/2 - a)]. \tag{6.9}$$

Next, we express Φ_0 from Eq. (6.9) and substitute the result in Eq. (6.7); after some transformations, we obtain:

$$\frac{u_{\text{el}}(r)}{kT} = \frac{r}{4L_{\text{B}}}[\Phi(r/2)]^2 \tag{6.10}$$

($r = L$). In our numerical calculations, the computed $\Phi(r)$ curves (like those shown in Figs. 8 and 9; see Appendix A) were converted into $u_{\text{el}}(r)$ dependencies with the help of Eq. (6.10); next, $u_{\text{el}}(r)$ was substituted in Eq. (6.4) to calculate d_{eff} by numerical integration. The results are as follows.

Illustrative $u_{\text{el}}(r)$-dependencies are shown in Fig. 14a for the interaction between two CPC micelles at different surfactant concentrations, c_s. The JA model has been used. With the rise of c_s, κ increases, see Eq. (3.3), and consequently the energy of electrostatic repulsion, $u_{\text{el}}(r)$, decreases. In addition, Fig. 14b shows the respective values of the function

$$f(r) = 1 - exp\left(-\frac{u(r)}{kT}\right), \tag{6.11}$$

which is present in the integrand of Eq. (6.1); see also Eq. (6.3). At shorter interparticle distances ($2 < r/a < 3$), where $u_{\text{el}}/(kT) \gg 1$, we have $f(r) \approx 1$; compare Fig. 14a and b. In other words, $f(r)$ and the integral in Eq. (6.4) that expresses d_{eff} are not sensitive to the exact value of u_{el} in the region of short distances and high potentials. However, both $f(r)$ and d_{eff} are sensitive to the behavior of u_{el} at longer distances ($r/a > 3$) and low potentials, where the asymptotic expressions, Eqs. (6.7) and (6.10), are accurate. The latter fact explains why d_{eff} can be accurately calculated using only the asymptotics of $u_{\text{el}}(r)$ at not-too-short distances, despite the circumstance that Eq. (6.1) contains integration over all distances ($0 < r < \infty$).

Fig. 15a compares the experimental values of Δh for SDS (see Fig. 4) with the theoretical curves $\Delta h = d_{\text{eff}}(c_s)$ calculated using Eqs. (6.4) and (6.10), the latter with $\Phi(r/2)$ computed in the framework of two different models: PB and JA (see Section 4). It is

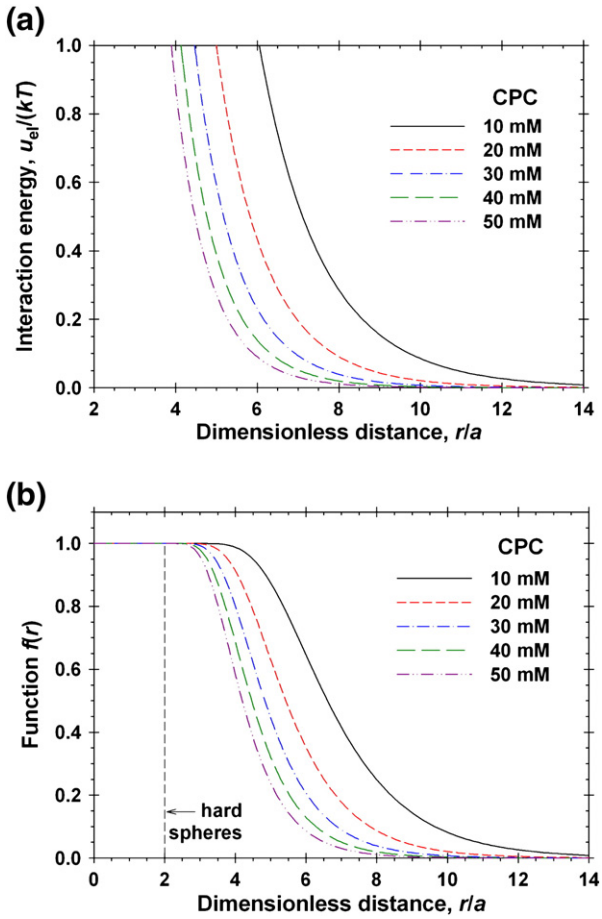

Fig. 14. (a) Dimensionless energy of electrostatic repulsion between two micelles, $u_{el}(r)/kT$, calculated from Eq. (6.10) by the JA model for several CPC concentrations as explained in the text. (b) The function $f(r)$ calculated from the above $u_{el}(r)/kT$ curves with the help of Eq. (6.11).

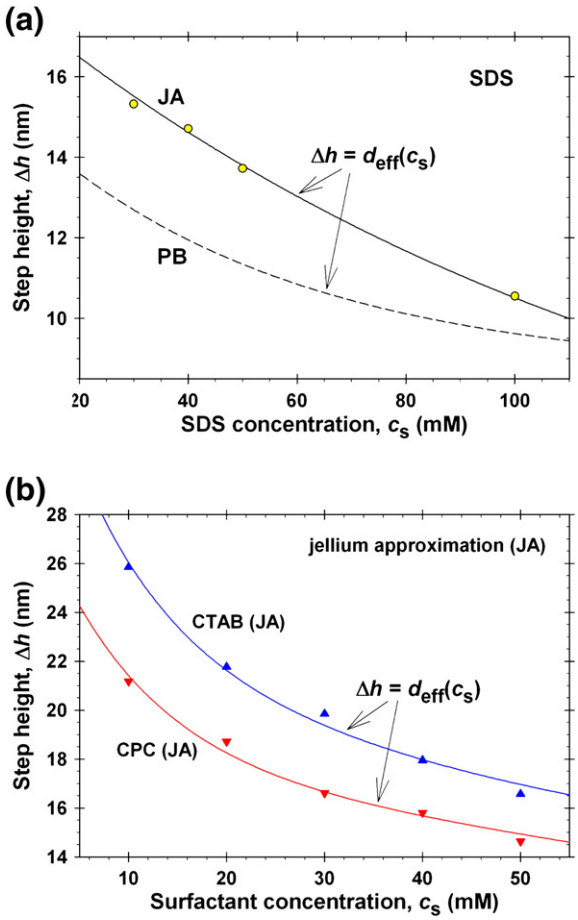

Fig. 15. Plots of the step height, Δh, vs. the surfactant concentration, c_s. The points are data from Fig. 4; the solid lines are theoretical curves calculated by means of the JA model without using any adjustable parameter. (a) Comparison of the data for SDS with the predictions of the JA model (solid line) and PB model (dashed line). (b) Comparison of the data for CTAB and CPC with the predictions of the JA model.

seen that the theoretical curve predicted by the JA model is in excellent agreement with the experiment (no adjustable parameters). In contrast, the PB model predicts considerably smaller Δh, which can be explained with the stronger screening of the electrostatic interactions because of the greater value of the screening parameter κ_{PB}; compare Eqs. (4.12) and (4.17).

Fig. 15b shows that an excellent agreement between the theory based on the JA model and the experiment is present also in the cases of CTAB and CPC (no adjustable parameters). For all three surfactants, the values of N_{agg} have been taken from Table 4, whereas the $\alpha(c_s)$ dependencies are those in Fig. 10 for the JA model.

In general, the results for Δh (Fig. 15) indicate that the JA model adequately describes the interaction between the micelles, whereas the PB model underestimates the interaction energy. We did not use the cell model to calculate d_{eff}, because Eq. (6.4) includes integration over the whole range of distances, whereas the cell model gives $\Phi(r)$ only inside the cell, i.e. for $a<r<b$. If the definition of Φ is extended as $\Phi(r)=0$ for $r>b$, then in view of Fig. 9 and Eq. (6.10) the CM would predict the smallest d_{eff} among the three considered models.

6.3. Osmotic approach to the interpretation of Δh

Another, completely different approach to the interpretation of the magnitude, Δh, of the stepwise transitions in the film thickness is related to the observation by Nikolov et al. [3–5] that the experimental values of Δh for micellar SDS solutions is approximately equal to the average distance, δ_l, between two micelles in the bulk of solution:

$$\Delta h \approx \delta_l \equiv \left(c_{p\infty}\right)^{-1/3} = \left(\frac{c_s - \mathrm{CMC}}{N_{agg}}\right)^{-1/3}, \tag{6.12}$$

see Table 1 in Ref. [3], or Table III in Ref. [4]. Later, analogous results have been obtained by Walz et al. [26,27] for silica nanoparticles. The most probable explanation of this experimental finding is the following. Because of the large number of dissociated counterions, the micelles (the charged particles) give a considerable contribution to the osmotic pressure of the solution. The latter is much greater than the applied capillary pressure P_c (see Table 5) and the van der Waals component of disjoining pressure, Π_{vw}, which is also small in view of the larger thickness of films that contain charged micelles. For this reason, at equilibrium the osmotic pressures of the micelles in the film and in the bulk must be approximately equal, and consequently, the respective average micelle concentrations have to be practically the same.

From Eq. (6.12), we obtain the following expression for the micelle mean aggregation number:

$$N_{agg} \approx (c_s - \mathrm{CMC})(\Delta h)^3. \tag{6.13}$$

With the help of Eq. (6.13), we calculated N_{agg} substituting the experimental Δh at different surfactant concentrations c_s for the three

investigated surfactants (Fig. 15). The used values of CMC are 8, 0.9 and 1 mM, respectively, for SDS, CTAB and CPC. The results are given in Table 6, where the last column contains literature data for N_{agg}. As seen, the predictions of Eq. (6.13) agree well with the literature data.

Eq. (6.12) implicitly assumes that the micelles are spherical, so that the method based on Eq. (6.13) is applicable only to spherical micelles. From this viewpoint, the largest values of N_{agg} for CTAB in Table 6 might correspond to elongated micelles, so that the calculated N_{agg} might not be so accurate.

In general, Eq. (6.13) predicts that N_{agg} increases with the rise of surfactant concentration (Table 6), which was found for nonionic surfactants [19,38] and for SDS as well [69]. The predictions of this equation should be tested against additional data for N_{agg} obtained by other methods.

Another way to test the osmotic approach is to use experiments with solid particles, for which the complications with the variable micelle aggregation number do not exist. Such experiments have been already carried out by colloidal-probe-atomic-force microscopy (CP-AFM) and by Monte Carlo (MC) simulations [36], and it was established that $\Delta h \sim (\phi)^{-1/3}$ with ϕ being the particle volume fraction. (In the CP-AFM experiments, Δh is the period of the measured oscillatory force.) The diameter of the used silica particles was $2a = 25$ nm in [36]. In view of Eq. (6.12), we can predict the coefficient in the dependence $\Delta h \sim (\phi)^{-1/3}$, viz.

$$\Delta h = \left(c_{p\infty}\right)^{-1/3} = \left(\frac{4}{3}\pi\right)^{1/3} a\ \phi^{-1/3} \approx 1.612\ a\phi^{-1/3}. \tag{6.14}$$

To check this prediction, in Fig. 16 we have plotted (as Δh vs. $\phi^{-1/3}$) the data from Fig. 3a in Ref. [36] from both the CP-AFM measurements and MC simulations. As seen in Fig. 16, these data excellently agree with a straight line of coefficient $1.612a$. This is an additional argument in favor of the osmotic approach.

The method based on the osmotic approach, namely, Δh measurements and use of Eq. (6.13), could become one of the most convenient and reliable methods for determining the aggregation number of spherical micelles in ionic surfactant solutions.

6.4. Discussion

The *energy* approach to the interpretation of Δh (Sections 6.1 and 6.2) is based on the relation $\Delta h = d_{eff}$, where the effective diameter of the micelles (charged particles) is determined by the energy of electrostatic interparticle repulsion through the second virial coefficient; see Eq. (6.4). Following this approach, we were able

Table 6
Micelle aggregation number, N_{agg}, calculated from Eq. (6.13) vs. literature data for N_{agg}.

c_s (mM)	Δh (nm)	N_{agg} from Eq. (6.13)	N_{agg} from literature
SDS			
30	15.32	48	50 [68], 59 [69]
40	14.71	61	64 [69]
50	13.72	65	64 [68,69]
100	10.55	65	65 [77], 70 [68]
CTAB			
10	25.85	95	88 [77], 95 [169]
20	21.77	119	–
30	19.86	137	100 [169]
40	17.95	136	–
50	16.57	135	139 [85], 140 [169]
CPC			
10	21.18	52	45–90 [87]
20	18.72	75	78 (Table 4)
30	16.61	80	–
40	15.80	93	–
50	14.64	93	87 [90]

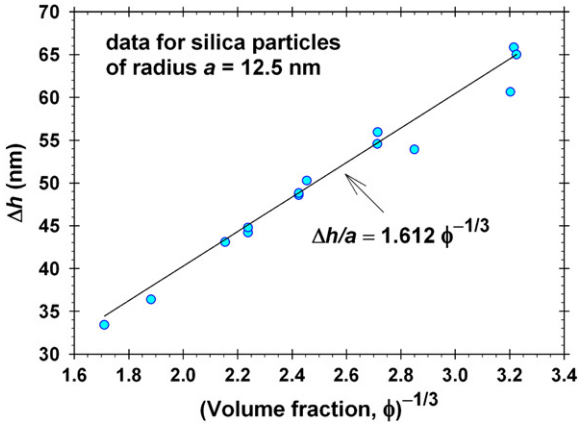

Fig. 16. Plot of Δh vs. $\phi^{-1/3}$, where ϕ is the volume fraction of silica particles. The points are data from Fig. 3 in Ref. [36]. The straight line is drawn in accordance with Eq. (6.14).

to interpret the data for Δh vs. c_s (Fig. 15) using a fixed aggregation number for all c_s values (see Table 4).

The *osmotic* approach to the interpretation of Δh (Section 6.3), which is based on the relation $\Delta h = (c_{p\infty})^{-1/3}$, relates the stratification steps to the mean distance between the micelles in the bulk and gives an increase in N_{agg} with the rise of surfactant concentration, c_s (Table 6).

It is interesting that both approaches are consistent with a simple-cubic-lattice packing of the micelles in the film. Indeed, if the packing of the micelles was hexagonal, then we should have $\Delta h = (2/3)^{1/2} d_{eff}$ [40]. Likewise, the relation $\delta_l = (c_{p\infty})^{-1/3}$ in Eq. (6.12) also presumes simple-cubic-lattice packing. For the time being, it is unclear whether this result is just a feature of the considered models or it reflects the real packing structure of the charged particles within the plane-parallel thin films. The Monte Carlo simulations of the structuring of charged colloid particles confined between two walls gave simple cubic packing for mica walls with surface potential $\psi_s = 160$ mV, however, hexagonal packing was obtained for silica walls with $\psi_s = 80$ mV [58].

As already mentioned, $d_{eff} = \delta_l$ for the experimental systems studied by us. However, if electrolyte is added to the micellar surfactant solution, d_{eff} should decrease because the micelle counter-ion atmosphere shrinks. In contrast, δ_l should remain (almost) constant if the variation of N_{agg} with the salt concentration is not so significant for spherical micelles. To illustrate the effect of electrolyte, in Fig. 17 we have plotted $\delta_l = (c_{p\infty})^{-1/3}$ and d_{eff} computed by means of the full procedure described in Section 6.2. The calculations are carried out for micellar solutions of CPC, using the respective values of K_{St}, a and N_{agg} from Tables 1 and 4.

As seen in Fig. 17, $d_{eff} = \delta_l$ at the lower concentrations of NaCl. At higher salt concentrations, we have $d_{eff} < \delta_l$. Thus, d_{eff} becomes equal to 90% of δ_l at 0.71 and 3.9 mM NaCl, respectively, for $c_s = 10$ and 50 mM CPC. Our results (the agreement between the JA-based theory and the experiment in Figs. 12b and 15 without using any adjustable parameters) indicate that in the first region, where $d_{eff} = \delta_l$, the micellar solution behaves as a jellium, i.e. the concentration of the micelles remains uniform even if an electric-double-layer field is present, as sketched in Fig. 18a. In other words, our experimental data (Figs. 3 and 4), corresponding to $c_{3\infty} = 0$, belong to the *jellium region*. In this region, the micelles together with their counterion atmospheres could be considered as soft, compressible particles, which can accommodate their diameter, d_{eff}, to the available distance between the particles, $\delta_l = (c_{p\infty})^{-1/3}$, which is determined by the micelle concentration (Fig. 18a). For this reason, in the jellium region the JA model is the best among the three models considered in Section 4. The term "jellium" originates from the quantum theory of electron gas in metals (solid state physics) [180] and it was introduced in colloid

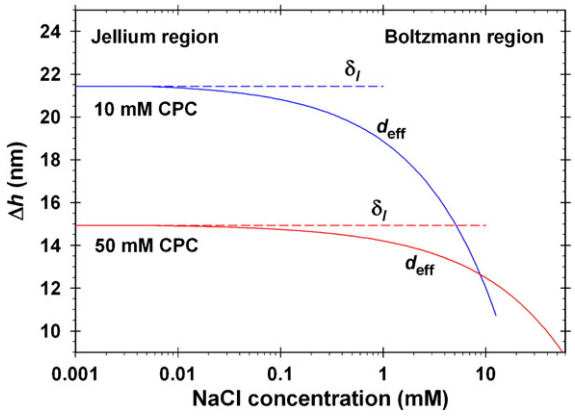

Fig. 17. Effect of NaCl concentration, $c_{3\infty}$, on the effective diameter, d_{eff}, of the counterion atmospheres of CPC micelles at two surfactant concentrations denoted in the figure: Theoretical curves calculated using the values of K_{St}, a and N_{agg} for CPC (details in the text). At lower salt concentrations, d_{eff} coincides with the mean distance between the micelles, $\delta_l = (c_{p\infty})^{-1/3}$ (jellium region). At higher salt concentrations, we have $d_{eff} < \delta_l$ (Boltzmann region).

science (interactions between charged particles in suspensions) by Beresford-Smith et al. [61,62].

The region with $d_{eff} < \delta_l$ in Fig. 17 corresponds to a system of particles, in which counterion atmospheres are not pressed to each other, i.e. the mean distance between the particles, δ_l, is greater than the effective diameter, d_{eff}, of their counterion atmospheres (Fig. 18b). If a double-layer electric field is present, the particles (micelles) will obey the Boltzmann distribution. This *Boltzmann region* can be realized at sufficiently high concentrations of added electrolyte

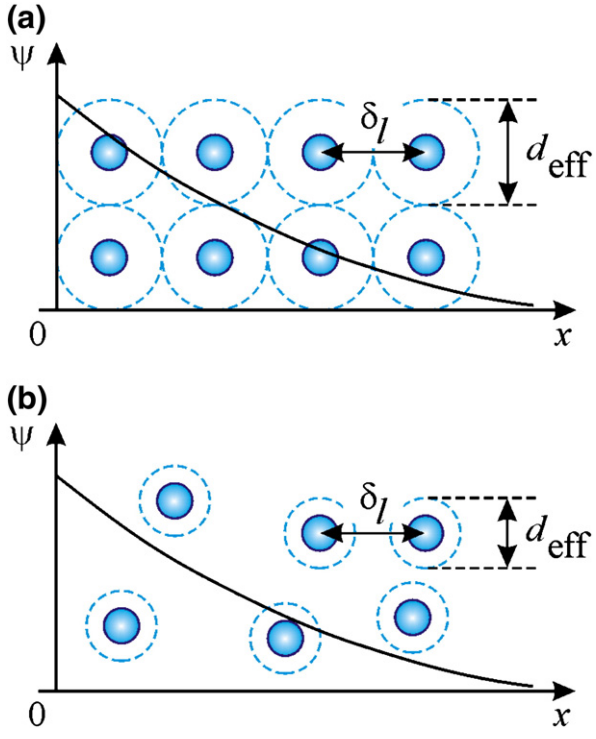

Fig. 18. (a) In the *jellium region* ($d_{eff} = \delta_l$), the micelles together with their counterion atmospheres could be considered as soft, compressible particles, which accommodate their diameter, d_{eff}, to the available distance between the particles that is determined by the micelle concentration, $\delta_l = (c_{p\infty})^{-1/3}$. If the applied electric field ψ is not too strong, it does not affect the uniform distribution of the micelles so that the jellium approximation is applicable (see Section 4.3). (b) In the *Boltzmann region* ($d_{eff} < \delta_l$), the effective diameter of the micelles, d_{eff}, is smaller than the average distance between them, δ_l, so that they obey the Boltzmann distribution in external field, ψ.

(Fig. 17), or at sufficiently low particle (micelle) concentrations [35]. As a rule, in such cases stepwise thinning of liquid films (stratification) is not observed. Therefore, we could hypothesize that the boundary between the "jellium" ($d_{eff} = \delta_l$) and "Boltzmann" ($d_{eff} < \delta_l$) regions corresponds to the boundary between stratifying and non-stratifying films.

7. Summary and conclusions

In this article, we investigated the stepwise thinning of aqueous films containing electrically charged colloidal particles, in our case — surfactant micelles. Although the paper is focused on micellar solutions, most of the results are applicable also to films from nanoparticle suspensions.

To test different theoretical approaches, we obtained experimental data for the stepwise thinning of free foam films from solutions of three ionic surfactants (see Figs. 2 and 3). The film thickness at each of the film's metastable states was determined as a function of the total surfactant concentration (Fig. 4). The experiment indicates that heights of the steps are equal: $h_3 - h_2 \approx h_2 - h_1 \approx h_1 - h_0 = \Delta h$. Thus, the theoretical problem is reduced to the interpretation of the experimental dependencies of Δh and h_0 on the surfactant concentration c_s.

Because the electrostatic interactions between the micelles play a central role, it is important to know the degree of micelle ionization, α. However, different experimental methods give rather different values of α [64]. The problem can be solved by using the Stern model, which considers the binding (condensation) of counterions at the charged groups on the micelle surface. The values of the Stern constant, K_{St}, used in this paper (Table 1) are determined from fits of data for the surface tension as a function of the surfactant and salt concentrations (see e.g. Fig. 6). After that, α was calculated as a function of c_s (Fig. 10). The obtained values of α are close to those determined by electrolytic conductivity experiments (Fig. 7).

To calculate α from K_{St} and to interpret the experimental h_0 and Δh, an adequate theoretical model has to be applied. The applicability of three models was tested. The first one is the conventional Poisson–Boltzmann (PB) model that assumes Boltzmann distribution of the micelles in the electric field of a selected micelle in the solution. In this case, the Debye parameter κ_{PB} includes a contribution from the micelles as multivalent ions, Eq. (4.12). The second is the jellium-approximation (JA), which assumes a uniform distribution of the micelles around each selected micelle in the solution. In this case, the Debye parameter κ includes contributions only from the small ions, Eq. (4.17). The third is the cell model (CM), which considers separately each micelle together with its counterion atmosphere as a cell of volume equal to the volume per micelle in the solution.

The best agreement with the experiment was obtained with the JA model, which gives excellent agreement with the experimental data for $h_0(c_s)$ and $\Delta h(c_s)$ without using any adjustable parameters; see Figs. 12b and 15. In contrast, the PB model is not in quantitative agreement with the experiment; see e.g. Fig. 15a. From this viewpoint, the values of α predicted by the JA model can be considered as the most realistic. In contrast, the CM model gives the worst predictions for α among the three investigated models (Fig. 10).

The thinnest stable films (those of thickness h_0 in Fig. 4), which have been experimentally observed, are thick enough to contain surfactant micelles. The comparison of theory and experiment with respect to h_0 (Section 5) reveals that these films really contain micelles (at a very low concentration) to ensure the osmotic balance between the film and the bulk solution. Furthermore, two approaches to the interpretation of the step height Δh have been proposed. In the *energy approach*, Δh is identified with the effective diameter of the charged particle, d_{eff}, which is determined by the second virial coefficient; see Sections 6.1 and 6.2. In the *osmotic approach*, $\Delta h = \delta_l$, where $\delta_l = (c_{p\infty})^{-1/3}$ is the mean distance between two micelles in the bulk (Section 6.3).

For the considered experimental systems (no added salt), the energy and osmotic approaches give coinciding predictions, which coincide also with the experimental height of the step, i.e. $d_{\rm eff}=\delta_l=\Delta h$; see Figs. 15b and 17. This coincidence and the excellent performance of the JA model mean that the micellar phase in the bulk of solution and in the liquid film represents a jellium, i.e. the electrostatic repulsion between the micelles (particles) leads to their uniform distribution. In this respect, the micelles, together with their counterion atmospheres behave as soft balls that adjust their size in accordance with the volume per micelle, which equals the inverse micellar number density (Fig. 18a). However, upon addition of electrolyte (or at low micelle concentrations) we have $d_{\rm eff}<\delta_l$ (Fig. 17), which means that the counterion atmospheres of the micelles are no longer pressed against each other, and then the solution cannot be considered as a jellium (Fig. 18b). This is the limit of applicability of the models presented here, but as a rule, beyond this limit stepwise film-thickness transitions are not experimentally observed.

In brief, the predictions of the energy and osmotic approaches to stratification coincide because (and wherever) the dispersion of charged particles behaves as a jellium. Conversely, it is possible to judge whether a jellium distribution is present by the coincidence of the predictions of these two approaches with respect to Δh.

Finally, it is worthwhile mentioning that in the jellium region, where stepwise transitions are observed, the aggregation number of spherical charged micelles can be determined from the experimental step height, Δh; see Table 6 and Eq. (6.13).

Acknowledgments

We thankfully acknowledge the support from the National Science Fund of Bulgaria, grant no. DID-02-18/2009; from Unilever R&D, Trumbull, USA, and from COST Action D43 of ESF. The authors are grateful to Dr. Mariana Boneva for measuring the electrolytic conductivity of the SDS and CTAB solutions.

Appendix A. Principles of the numerical procedure for the electrostatic potential

Let us consider the equation:

$$\frac{\partial\Phi}{\partial\tau}=\frac{\partial^2\Phi}{\partial\chi^2}+\frac{2}{\chi}\frac{\partial\Phi}{\partial\chi}-F_{\rm b}(\alpha,\Phi). \tag{A.1}$$

Here, as usual, Φ is the dimensionless electrostatic potential, Eq. (4.3); $\chi\equiv r/a$ is a dimensionless radial distance; τ is a dimensionless numerical time of iterations, and $F_{\rm b}$ represents the right-hand side of either of Eqs. (4.10), (4.15) or (4.18). The stationary solution, for which the left-hand side of Eq. (A.1) is equal to zero, represents the solution of our boundary problem. The boundary condition at the particle (micelle) surface is:

$$\frac{\partial\Phi}{\partial\chi}=F_{\rm s}(\alpha)\ \text{ at }\ \chi=1 \tag{A.2}$$

where $F_{\rm s}(\alpha)=-\alpha N_{\rm agg}L_{\rm B}/a$ for ionic micelles; see Eq. (4.4). In the case of PB and JA models, to avoid the use of a boundary condition at infinity, we employed Eq. (4.20) that expresses the known asymptotic solution for $\Phi\ll 1$. Differentiating Eq. (4.20) with respect to r, we obtain the following linear boundary condition:

$$\frac{d\Phi}{dr}+\left(\kappa+\frac{1}{r}\right)\Phi=0\quad\text{at}\quad r=a_\infty\ \text{ for JA and PB} \tag{A.3}$$

where κ is given by Eq. (4.17) for the JA model, and $\kappa=\kappa_{\rm PB}$ for the PB model, Eq. (4.12); in our computations, a_∞, was chosen in such a way that $[\exp(-\kappa a_\infty)]/(\kappa a_\infty)=10^{-16}$. In the case of CM, the boundary condition at the outer cell boundary reads

$$\frac{d\Phi}{dr}=0\quad\text{at}\quad r=b\quad\text{for CM.} \tag{A.4}$$

The boundary conditions, Eqs. (A.3) and (A.4), can be presented in the following general form

$$\frac{\partial\Phi}{\partial\chi}=\beta\Phi\quad\text{at}\ \chi=\tilde{b}\equiv\frac{a_\infty}{a}\ \text{ or }\ \frac{b}{a} \tag{A.5}$$

where $\tilde{b}$ is the boundary of the numerical domain and β is a constant ($\beta=-\kappa a_\infty-1$ or 0).

To avoid the slow oscillatory relaxation of the Crank–Nicholson scheme, we used the idea of the Keller box numerical scheme [181,182] and replaced the second-order differential equation with a system of two first-order equations for the functions X and Y defined as follows:

$$X\equiv\Phi\quad\text{and}\quad Y\equiv\frac{\partial\Phi}{\partial\chi}. \tag{A.6}$$

With the help of Eq. (A.6), we bring Eq. (A.1) in the form:

$$\frac{\partial X}{\partial\tau}=\frac{\partial X}{\partial\chi}+\frac{2}{\chi}Y-F_{\rm b}(\alpha,X) \tag{A.7a}$$

$$\frac{\partial X}{\partial\chi}=Y \tag{A.7b}$$

for $1<\chi<\tilde{b}$ and $\tau>0$, with boundary conditions:

$$Y=F_{\rm s}(\alpha)\ \text{at}\ \chi=1\quad\text{and}\ \tau>0 \tag{A.8a}$$

$$Y=\beta X\quad\text{at}\ \chi=\tilde{b}\quad\text{and}\ \tau>0. \tag{A.8b}$$

As initial conditions (at $\tau=0$), we used the respective solutions of the linearized problems, $X_0(\chi)$ and $Y_0(\chi)$.

In what follows, the subscripts k, $k+1/2$, and $k+1$ denote the values of a given function calculated at time moments $k\Delta\tau$, $(k+1/2)\Delta\tau$, and $(k+1)\Delta\tau$, respectively, where $\Delta\tau$ is the numerical time step. Eq. (A.7a) is replaced with its second-order-precision difference scheme:

$$\frac{X_{k+1}-X_k}{\Delta\tau}=\frac{\partial X_{k+1/2}}{\partial\chi}+\frac{2}{\chi}Y_{k+1/2}-F_{\rm b}\left(\alpha_{k+1/2},X_{k+1/2}\right) \tag{A.9}$$

for $1<\chi<\tilde{b}$. Furthermore, the functions in Eq. (A.9) are calculated in the half-time node, keeping the second order precision of the numerical scheme:

$$\frac{X_{k+1}-X_k}{\Delta\tau}=\frac{1}{2}\frac{\partial X_{k+1}}{\partial\chi}+\frac{1}{2}\frac{\partial X_k}{\partial\chi}+\frac{Y_{k+1}+Y_k}{\chi}-F_{\rm b}\left(\frac{\alpha_{k+1}+\alpha_k}{2},\frac{X_{k+1}+X_k}{2}\right) \tag{A.10}$$

for $1<\chi<\tilde{b}$. The nonlinear function $F_{\rm b}$ in the right-hand side of the latter equation is linearized by using the Newton method with second order precision:

$$F_{\rm b}\left(\frac{\alpha_{k+1}+\alpha_k}{2},\frac{X_{k+1}+X_k}{2}\right)=F_{\rm b}\Big|_{\alpha_k,X_k}+\frac{\partial F_{\rm b}}{\partial\alpha}\Big|_{\alpha_k,X_k}\frac{\partial\alpha}{\partial X}\Big|_{X_k(1)}\frac{X_{k+1}(1)-X_k(1)}{2}+\frac{\partial F_{\rm b}}{\partial X}\Big|_{\alpha_k,X_k}\frac{X_{k+1}-X_k}{2}. \tag{A.11}$$

From Eqs. (A.7b) and (A.10), along with Eq. (A.11), we obtain the following linear system of equations for the functions at the moment $(k+1)\Delta\tau$:

$$\frac{X_{k+1}-X_k}{\Delta\tau} = \frac{1}{2}\frac{\partial X_{k+1}}{\partial\chi} + \frac{1}{2}\frac{\partial X_k}{\partial\chi} + \frac{Y_{k+1}+Y_k}{\chi} - F_b\Big|_{\alpha_k,X_k} - \frac{\partial F_b}{\partial\alpha}\Big|_{\alpha_k,X_k}\frac{\partial\alpha}{\partial X}\Big|_{X_k(1)}\frac{X_{k+1}(1)-X_k(1)}{2} - \frac{\partial F_b}{\partial X}\Big|_{\alpha_k,X_k}\frac{X_{k+1}-X_k}{2} \tag{A.12}$$

$$\frac{\partial X_{k+1}}{\partial\chi} = Y_{k+1} \tag{A.13}$$

for $1<\chi<\tilde{b}$. The boundary condition, Eq. (A.8a), can be written at the half-time step:

$$Y_{k+1/2} = F_s\left(\alpha_{k+1/2}\right)\text{at }\chi = 1. \tag{A.14}$$

In Eq. (A.14), the functions calculated in the half-time node can be replaced with their mean values keeping the second order precision:

$$\frac{Y_{k+1}+Y_k}{2} = F_s\left(\frac{\alpha_{k+1}+\alpha_k}{2}\right)\text{at }\chi = 1. \tag{A.15}$$

In the right-hand side of the latter equation, we expand F_s in analogy with Eq. (A.11):

$$Y_{k+1}(1)+Y_k(1) = 2F_s\Big|_{\alpha_k,X_k} + \frac{\partial F_s}{\partial\alpha}\Big|_{\alpha_k}\frac{\partial\alpha}{\partial X}\Big|_{X_k(1)}\left[X_{k+1}(1)-X_k(1)\right]. \tag{A.16}$$

The boundary condition Eq. (A.8b) can be expressed in the form:

$$Y_{k+1}\left(\tilde{b}\right) = \beta X_{k+1}\left(\tilde{b}\right). \tag{A.17}$$

The linear system of equations, Eqs. (A.12)–(A.13), is solved by introducing a uniform grid with respect to χ, with a step $\Delta\chi=(\tilde{b}-1)/N$, where N is the number of space intervals. We are using superscripts n, $n+1/2$, and $n+1$ to denote the function calculated at nodes $1+n\Delta\chi$, $1+(n+1/2)\Delta\chi$, and $1+(n+1)\Delta\chi$, respectively. Thus, for the half-space node Eq. (A.12) acquires the form:

$$\left(\frac{1}{2}\frac{\partial F_b}{\partial X}\Big|_{\alpha_k,X_k} + \frac{1}{\Delta\tau}\right)\left(X_{k+1}^{n+1/2}-X_k^{n+1/2}\right) = \frac{X_{k+1}^{n+1}-X_{k+1}^n}{2\Delta\chi} + \frac{X_k^{n+1}-X_k^n}{2\Delta\chi} + \frac{Y_{k+1}^{n+1/2}+Y_k^{n+1/2}}{\chi^{n+1/2}} - F_b\Big|_{\alpha_k,X_k} - \frac{1}{2}\frac{\partial F_b}{\partial\alpha}\Big|_{\alpha_k,X_k}\frac{\partial\alpha}{\partial X}\Big|_{X_k(1)}\left(X_{k+1}^0-X_k^0\right) \tag{A.18}$$

for $n=0, 1, 2, \ldots, N-1$. Replacing the values at the half-space node with their mean values, we obtain:

$$\left(\frac{1}{4}\frac{\partial F_b}{\partial X}\Big|_{\alpha_k,X_k} + \frac{1}{2\Delta\tau}\right)\left(X_{k+1}^{n+1}+X_{k+1}^n-X_k^{n+1}-X_k^n\right) = \frac{X_{k+1}^{n+1}-X_{k+1}^n}{2\Delta\chi} + \frac{X_k^{n+1}-X_k^n}{2\Delta\chi} + \frac{Y_{k+1}^{n+1}+Y_{k+1}^n+Y_k^{n+1}+Y_k^n}{2\chi^{n+1/2}} - F_b|_{\alpha_k,X_k} - \frac{1}{2}\frac{\partial F_b}{\partial\alpha}|_{\alpha_k,X_k}\frac{\partial\alpha}{\partial X}|_{X_k(1)}\left(X_{k+1}^0-X_k^0\right) \tag{A.19}$$

for $n=0, 1, 2, \ldots, N-1$. Likewise, Eq. (A.13) acquires the form:

$$\frac{X_{k+1}^{n+1}-X_{k+1}^n}{\Delta\chi} = \frac{Y_{k+1}^{n+1}+Y_{k+1}^n}{2}\text{ for }n=0,1,2,\ldots,N-1. \tag{A.20}$$

The matrix of the linear system of equations, Eqs. (A.16), (A.17), (A.19) and (A.20), has a three-diagonal form with a nonzero first column, because of the term with X_{k+1}^0 in Eq. (A.19). There is a simple and exact rule for inverting such matrices, which was used in our program. The numerical method fast converges to the stationary solution, which represents the solution of the considered boundary problem. To achieve a good precision, we used a large number of intervals, $N=10^5$.

Appendix B. Derivation of the expression for the interaction force

Let us consider two identical spherical particles separated at a center-to-center distance L, see Fig. 13. The origin of the Cartesian coordinate system is located in the middle between the particles, so that their centers have coordinates $(-L/2,0,0)$ and $(L/2,0,0)$. The electric force, F, acting on the particle 2 (Fig. 13) is given by the expression:

$$\mathbf{F} = \int_S \mathbf{P}\cdot\mathbf{n}dS \tag{B.1}$$

$\mathbf{n}$ is the running unit normal vector to the surface S of this particle; the Maxwell pressure tensor, P, is defined as follows [126]:

$$\mathbf{P} \equiv \left(p + \frac{\varepsilon}{8\pi}\nabla\psi\cdot\nabla\psi\right)\mathbf{U} - \frac{\varepsilon}{4\pi}\nabla\psi\nabla\psi \tag{B.2}$$

where $\mathbf{U}$ is the spatial unit tensor; ∇ is the del operator, and p is the scalar pressure. As before, ψ is the electrostatic potential and we assume that the small ions are monovalent, whereas the particles (micelles) have a charge of magnitude Z (in electronic-charge units).

(a) Poisson Boltzmann (PB) model. In this model, the pressure p and the bulk charge density ρ_b are given by the expressions:

$$\frac{p-p_0}{kT} = 2(\text{CMC}+c_{3\infty})\,cosh\Phi + Zc_{p\infty}e^{\Phi} + c_{p\infty}e^{-Z\Phi} \tag{B.3}$$

$$\frac{\rho_b}{ze} = -2(\text{CMC}+c_{3\infty})\,sinh\Phi - Zc_{p\infty}e^{\Phi} + Zc_{p\infty}e^{-Z\Phi}. \tag{B.4}$$

Here, p_0 is a constant pressure; Φ is the dimensionless surface potential defined by Eq. (4.3); $z=+1$ or -1, respectively, for positively or negatively charged particle (micelle); with this definition, we have $\Phi\geq 0$. With the help of Eqs. (B.2)–(B.4), one can verify that the equation $\nabla\cdot\mathbf{P}=0$ is equivalent to the Poisson equation, Eq. (4.1). In other words, the condition for local mechanical equilibrium, $\nabla\cdot\mathbf{P}=0$, is fulfilled. Using the latter equation and the Gauss–Ostrogradsky divergence theorem, it can be proven that the integration in Eq. (B.1) over the surface of the particle 2 can be replaced by integration over the midplane, i.e. the yz-plane (Fig. 13):

$$\mathbf{F} = \int_{-\infty}^{\infty}\int_{-\infty}^{\infty}(\mathbf{P}\cdot\mathbf{e}_x - p_\infty\mathbf{e}_x)dydz \tag{B.5}$$

where p_∞ is the scalar pressure at a large distance from the particle (micelle) and $\mathbf{e}_x$ is the unit vector of the x-axis.. Because of the symmetry of the system only the x-component of $\mathbf{F}$ is different from zero, and then Eq. (B.5) reduces to

$$F_x = \int_{-\infty}^{\infty}\int_{-\infty}^{\infty}(P_{xx}-p_\infty)dydz = \int_{-\infty}^{\infty}\int_{-\infty}^{\infty}\left[p-p_\infty + \frac{\varepsilon}{8\pi}\left(\frac{\partial\psi}{\partial y}\right)^2 + \frac{\varepsilon}{8\pi}\left(\frac{\partial\psi}{\partial z}\right)^2\right]dydz\ \text{ at }\ x=0. \tag{B.6}$$

Integrating by parts, we obtain:

$$F_x = \int_{-\infty}^{\infty}\int_{-\infty}^{\infty}\left[p-p_\infty - \frac{\varepsilon\psi}{8\pi}\left(\frac{\partial^2\psi}{\partial y^2} + \frac{\partial^2\psi}{\partial z^2}\right)\right]dydz \quad \text{at} \quad x=0. \tag{B.7}$$

Using the Poisson equation, Eq. (4.1), we bring Eq. (B.7) in the form:

$$F_x = \int_{-\infty}^{\infty}\int_{-\infty}^{\infty}\left[p-p_\infty + \frac{\rho_b\psi}{2} + \frac{\varepsilon\psi}{8\pi}\frac{\partial^2\psi}{\partial x^2})\right]dydz \quad \text{at} \quad x=0. \tag{B.8}$$

At sufficiently large distances between the particles, the values of the dimensionless potential in the midplane between the particles are small, so that we can expand Eqs. (B.3) and (B.4) in a series for $\Phi|_{x=0} \ll 1$:

$$p-p_\infty = kT\left[2(\mathrm{CMC}+c_{3\infty}) + Zc_{p\infty} + Z^2c_{p\infty}\right]\frac{\Phi^2}{2} \tag{B.9}$$

$$\rho_b = -ze\left[2(\mathrm{CMC}+c_{3\infty}) + Zc_{p\infty} + Z^2c_{p\infty}\right]\Phi \tag{B.10}$$

at $x=0$. Substituting Eqs. (B.9) and (B.10) into Eq. (B.8), we establish that the contributions from the terms with $p-p_\infty$ and ρ_b cancel each other, and then Eq. (B.8) acquires the form:

$$F_x = \frac{kT}{8\pi L_B}\int_{-\infty}^{\infty}\int_{-\infty}^{\infty}\Phi\frac{\partial^2\Phi}{\partial x^2}dydz \quad \text{at} \quad x=0. \tag{B.11}$$

(b) Jellium approximation (JA). In this model, the bulk charge density ρ_b is given by the expression:

$$\frac{\rho_b}{ze} = -2(\mathrm{CMC}+c_{3\infty})\,sinh\Phi - Zc_{p\infty}e^{\Phi} + Zc_{p\infty}. \tag{B.12}$$

Substituting Eq. (B.2) into the local hydrostatic equilibrium equation $\nabla\cdot\mathrm{P}=0$, and using Eqs. (4.1) and (B.12), we obtain the expression for the pressure, p in the framework of the JA model:

$$\frac{p-p_0}{kT} = 2(\mathrm{CMC}+c_{3\infty})\,cosh\Phi + Zc_{p\infty}e^{\Phi} - Zc_{p\infty}\Phi. \tag{B.13}$$

Because the relationship $\nabla\cdot\mathrm{P}=0$ is fulfilled, Eqs. (B.5)–(B.8) hold again. Expanding Eqs. (B.12) and (B.13) in the midplane between the two particles for $\Phi|_{x=0} \ll 1$, we obtain:

$$\rho_b = -ze\left[2(\mathrm{CMC}+c_{3\infty}) + Zc_{p\infty}\right]\Phi \tag{B.14}$$

$$p-p_\infty = kT\left[2(\mathrm{CMC}+c_{3\infty}) + Zc_{p\infty}\right]\frac{\Phi^2}{2} \tag{B.15}$$

at $x=0$. Substituting Eqs. (B.14) and (B.15) into Eq. (B.8), we establish again that the contributions from the terms with $p-p_\infty$ and ρ_b cancel each other, and Eq. (B.8) reduces to Eq. (B.11). In other words, Eq. (B.11) holds for both the PB and JA models.

Insofar as the electrostatic potential in the midplane has been assumed to be low, we can apply the superposition approximation, $\Phi=\Phi_1+\Phi_2$, where Φ_1 and Φ_2 are the dimensionless electrostatic potentials created at a distance $L/2$ by each of the two particles in isolation. Substituting $\Phi=\Phi_1+\Phi_2$ in Eq. (B.11), we obtain the expression for the interaction force, Eq. (6.5).

References

[1] Johonnott ES. The black spots in thin liquid films. Philos Mag 1906;11:746–53.
[2] Perrin J. La stratification des lames liquides. Ann Phys-Paris 1918;10:160–84.
[3] Nikolov AD, Wasan DT, Kralchevsky PA, Ivanov IB. Ordered structures in thinning micellar foam and latex films. In: Ise N, Sogami I, editors. Ordering and organisation in ionic solutions. Singapore: World Scientific; 1988. p. 302–14.
[4] Nikolov AD, Wasan DT. Ordered micelle structuring in thin films from anionic surfactant solutions: I. Experimental. J Colloid Interface Sci 1989;133:1–12.
[5] Nikolov AD, Kralchevsky PA, Ivanov IB, Wasan DT. Ordered micelle structuring in thin films from anionic surfactant solutions: II. Model development. J Colloid Interface Sci 1989;133:13–22.
[6] Kralchevsky PA, Nikolov AD, Wasan DT, Ivanov IB. Formation and expansion of dark spots in stratifying foam films. Langmuir 1990;6:1180–9.
[7] Nikolov AD, Wasan DT, Denkov ND, Kralchevsky PA, Ivanov IB. Drainage of foam films in the presence of non-ionic micelles. Prog Colloid Polym Sci 1990;82:87–98.
[8] Wasan DT, Nikolov AD, Kralchevsky PA, Ivanov IB. Universality in film stratification due to colloid crystal formation. Colloids Surf 1992;67:139–45.
[9] Bergeron V, Radke CJ. Equilibrium measurements of oscillatory disjoining pressures in aqueous foam films. Langmuir 1992;8:3020–6.
[10] Bergeron V, Jimenez-Laguna AI, Radke CJ. Hole formation and sheeting in the drainage of thin liquid films. Langmuir 1992;8:3027–32.
[11] Richetti P, Kékicheff P. Direct measurements of depletion and structural forces of a micellar system. Phys Rev Lett 1992;68:1951–4.
[12] Parker JL, Richetti P, Kékicheff P, Sarman S. Direct measurement of structural forces in a supermolecular fluid. Phys Rev Lett 1992;68:1955–8.
[13] Horn RG, Israelachvili JN. Direct measurement of structural forces between two surfaces in a nonpolar liquid. J Chem Phys 1981;75:1400–11.
[14] Christenson HK, Gruen DWR, Horn RG, Israelachvili JN. Structuring in liquid alkanes between solid surfaces: force measurements and mean-field theory. J Chem Phys 1987;87:1834–41.
[15] Israelachvili JN, Pashley RM. Molecular layering of water at surfaces and origin of repulsive hydration forces. Nature 1983;306:249–50.
[16] Israelachvili JN. Intermolecular and surface forces. London: Academic Press; 1992.
[17] Sonin AA, Langevin D. Stratification dynamics of thin films made from aqueous micellar solutions. EPL-Europhys Lett 1993;22:271–7.
[18] von Klitzing R, Müller HJ. Film stability control. Curr Opin Colloid In 2002;7:42–9.
[19] Basheva ES, Kralchevsky PA, Danov KD, Ananthapadmanabhan KP, Lips A. The colloid structural forces as a tool for particle characterization and control of dispersion stability. Phys Chem Chem Phys 2007;9:5183–98.
[20] Wasan D, Nikolov A. Thin liquid films containing micelles or nanoparticles. Curr Opin Colloid In 2008;13:128–33.
[21] Krichevsky O, Stavans J. Micellar stratification in soap films: a light scattering study. Phys Rev Lett 1995;74:2752–5.
[22] Denkov ND, Yoshimura H, Nagayama K, Kouyama T. Nanoparticle arrays in freely suspended vitrified films. Phys Rev Lett 1996;76:2354–7.
[23] Denkov ND, Yoshimura H, Nagayama K. Method for controlled formation of vitrified films for cryo-electron microscopy. Ultramicroscopy 1996;65:147–58.
[24] Milling AJ, Kendall K. Depletion, adsorption, and structuring of sodium poly (acrylate) at the water–silica interface. Langmuir 2000;16:5108–15.
[25] Piech M, Walz JY. Direct measurement of depletion and structural forces in polydisperse, charged systems. J Colloid Interface Sci 2002;253:117–29.
[26] Piech M, Walz JY. The structuring of nonadsorbed nanoparticles and polyelectrolyte chains in the gap between a colloidal particle and plate. J Phys Chem B 2004;108:9177–88.
[27] Tulpar A, Van Tassel PR, Walz JY. Structuring of macroions confined between like-charged surfaces. Langmuir 2006;22:2876–83.
[28] McNamee CE, Tsujii Y, Matsumoto M. Interaction forces between two silica surfaces in an apolar solvent containing an anionic surfactant. Langmuir 2004;20:1791–8.
[29] McNamee CE, Tsujii Y, Ohshima H, Matsumoto M. Interaction forces between two hard surfaces in particle-containing aqueous systems. Langmuir 2004;20:1953–62.
[30] Biggs S, Prieve D, Dagastine R. Direct comparison of atomic force microscopic and total internal reflection microscopic measurements in the presence of nonadsorbing polyelectrolytes. Langmuir 2005;21:5421–8.
[31] Drelich J, Long J, Xu Z, Masliyah J, Nalaskowski J, Beauchamp R, Liu Y. AFM colloidal forces measured between microscopic probes and flat substrates in nanoparticle suspensions. J Colloid Interface Sci 2006;301:511–22.
[32] Qu D, Pedersen JS, Garnier S, Laschewsky A, Möhwald H, von Klitzing R. Effect of polymer charge and geometrical confinement on ion distribution and the structuring in semidilute polyelectrolyte solutions: comparison between AFM and SAXS. Macromolecules 2006;39:7364–71.
[33] Qu D, Brotons G, Bosio V, Fery A, Salditt T, Langevin D, von Klitzing R. Interactions across liquid thin films. Colloid Surface A 2007;303:97–109.
[34] Klapp SHL, Zeng Y, Qu D, von Klitzing R. Surviving structure in colloidal suspensions squeezed from 3D to 2D. Phys Rev Lett 2008;100:118303.
[35] Klapp SHL, Qu D, von Klitzing R. Long-range interactions between soft colloidal particles in slit–pore geometries. J Phys Chem B 2007;111:1296–303.
[36] Klapp SHL, Grandner S, Zeng Y, von Klitzing R. Asymptotic structure of charged colloids between two and three dimensions: the influence of salt. J Phys Condens Matter 2008;20:494232.
[37] Grandner S, Zeng Y, von Klitzing R, Klapp SHL. Impact of surface charges on the solvation forces in confined colloidal solutions. J Chem Phys 2009;131:154702.
[38] Christov NC, Danov KD, Zeng Y, Kralchevsky PA, von Klitzing R. Oscillatory structural forces due to nonionic surfactant micelles: data by colloidal-probe AFM vs. theory. Langmuir 2010;26:915–23.
[39] Basheva ES, Nikolov AD, Kralchevsky PA, Ivanov IB, Wasan DT. Multi-stepwise drainage and viscosity of macroscopic films formed from latex suspensions. In: Mittal KL, Shah DO, editors. Surfactants in solution, Vol. 11. New York: Plenum Press; 1991. p. 467–79.
[40] Basheva ES, Danov KD, Kralchevsky PA. Experimental study of particle structuring in vertical stratifying films from latex suspensions. Langmuir 1997;13:4342–8.
[41] Marinova KG, Gurkov TD, Dimitrova TD, Alargova RG, Smith D. Role of oscillatory structural forces for interactions in thin emulsion films containing micelles. Langmuir 1998;14:2011–9.

[42] Sethumadhavan GN, Nikolov AD, Wasan DT. Stability of liquid films containing monodisperse colloidal particles. J Colloid Interface Sci 2001;240:105–12.
[43] Bergeron V, Radke CJ. Disjoining pressure and stratification in asymmetric thin-liquid films. Colloid Polym Sci 1995;273:165–74.
[44] Dushkin CD, Nagayama K, Miwa T, Kralchevsky PA. Colored multilayers from transparent submicrometer spheres. Langmuir 1993;9:3695–701.
[45] Chengara A, Nikolov AD, Wasan DT, Trokhymchuk A, Henderson D. Spreading of nanofluids driven by the structural disjoining pressure gradient. J Colloid Interface Sci 2004;280:192–201.
[46] Nikolov AD, Kondiparty K, Wasan DT. Nanoparticle self-structuring in a nanofluid film spreading on a solid surface. Langmuir 2010;26:7665–70.
[47] Von Klitzing R, Thormann E, Nylander T, Langevin D, Stubenrauch C. Confinement of linear polymers, surfactants, and particles between interfaces. Adv Colloid Interface Sci 2010;155:19–31.
[48] Henderson D. An explicit expression for the solvent contribution to the force between colloidal particles using a hard sphere model. J Colloid Interface Sci 1988;121:486–90.
[49] Kjellander R, Sarman S. On the statistical mechanics of inhomogeneous fluids in narrow slits. An application to a hard-sphere fluid between hard walls. Chem Phys Lett 1988;149:102–8.
[50] Attard P, Parker JL. Oscillatory solvation forces: a comparison of theory and experiment. J Phys Chem 1992;96:5086–93.
[51] Pollard ML, Radke CJ. Density-functional modeling of structure and forces in thin micellar liquid films. J Chem Phys 1994;101:6979–91.
[52] Chu XL, Nikolov AD, Wasan DT. Monte Carlo simulation of inlayer structure formation in thin liquid films. Langmuir 1994;10:4403–8.
[53] Chu XL, Nikolov AD, Wasan DT. Thin liquid film structure and stability: the role of depletion and surface-induced structural forces. J Chem Phys 1995;103:6653–61.
[54] Trokhymchuk A, Henderson D, Nikolov AD, Wasan DT. Computer modeling of ionic micelle structuring in thin films. J Phys Chem B 2003;107:3927–37.
[55] Trokhymchuk A, Henderson D, Nikolov A, Wasan DT. Computer simulation of macroion layering in a wedge film. Langmuir 2005;21:10240–50.
[56] Blawzdziewicz J, Wajnryb E. Phase equilibria in stratified thin liquid films stabilized by colloidal particles. EPL-Europhys Lett 2005;71:269–75.
[57] Blawzdziewicz J, Wajnryb E. Equilibrium and nonequilibrium thermodynamics of particle-stabilized thin liquid films. J Chem Phys 2008;129:194509.
[58] Grandner S, Klapp SHL. Surface-charge-induced freezing of colloidal suspensions. EPL-Europhys Lett 2010;90:68004.
[59] Kralchevsky PA, Denkov ND. Analytical expression for the oscillatory structural surface force. Chem Phys Lett 1995;240:385–92.
[60] Trokhymchuk A, Henderson D, Nikolov A, Wasan DT. A simple calculation of structural and depletion forces for fluids/suspensions confined in a film. Langmuir 2001;17:4940–7.
[61] Beresford-Smith B, Chan DYC. Electrical double-layer interactions in concentrated colloidal systems. Faraday Discuss Chem Soc 1983;76:65–75.
[62] Beresford-Smith B, Chan DYC, Mitchell DJ. The electrostatic interaction in colloidal systems with low added electrolyte. J Colloid Interface Sci 1985;105:216–34.
[63] Henderson D, Trokhymchuk A, Nikolov A, Wasan DT. In-layer structuring of like-charged macroions in a thin film. Ind Eng Chem Res 2005;44:1175–80.
[64] Sasaki T, Hattori M, Sasaki J, Nukina K. Studies of aqueous sodium dodecyl sulfate solutions by activity measurements. Bull Chem Soc Jpn 1975;48:1397–403.
[65] Tajima K, Muramatsu M, Sasaki T. Radiotracer studies on adsorption of surface active substance at aqueous surface. I. Accurate measurements of adsorption of tritiated sodium dodecylsulfate. Bull Chem Soc Jpn 1970;43:1991–8.
[66] Tajima K. Radiotracer studies on adsorption of surface active substance at aqueous surface. II. The effect of excess salt on the adsorption of sodium dodecylsulfate. Bull Chem Soc Jpn 1970;43:3063–6.
[67] Tajima K. Radiotracer studies on adsorption of surface active substance at aqueous surface. III. The effect of salt on the adsorption of sodium dodecylsulfate. Bull Chem Soc Jpn 1971;44:1767–71.
[68] Bales BL, Almgren M. Fluorescence quenching of pyrene by Copper(II) in sodium dodecyl sulfate micelles. Effect of micelle size as controlled by surfactant concentration. J Phys Chem 1995;99:15153–62.
[69] Quina FH, Nassar PM, Bonilha JBS, Bales BL. Growth of sodium dodecyl sulfate micelles with detergent concentration. J Phys Chem 1995;99:17028–31.
[70] Bales BL, Messina L, Vidal A, Peric M, Nascimento OR. Precision relative aggregation number determinations of SDS micelles using a spin probe. A model of micelle surface hydration. J Phys Chem B 1998;102:10347–58.
[71] Mazer NA, Benedek GB, Carey MC. An investigation of the micellar phase of sodium dodecyl sulfate in aqueous sodium chloride using quasielastic light scattering spectroscopy. J Phys Chem 1976;80:1075–85.
[72] Missel PJ, Mazer NA, Benedek GB, Young CY. Thermodynamic analysis of the growth of sodium dodecyl sulfate micelles. J Phys Chem 1980;84:1044–57.
[73] Missel PJ, Mazer NA, Benedek GB, Carey MC. Influence of chain length on the sphere-to-rod transition in alkyl sulfate micelles. J Phys Chem 1983;87:1264–77.
[74] Tanford C. The hydrophobic effect. The formation of micelles and biological membranes. New York: Wiley; 1980.
[75] Hiemenz PC, Rajagopalan R. Principles of colloid and surface chemistry. New York: Marcel Dekker; 1997.
[76] Kralchevsky PA, Danov KD, Kolev VL, Broze G, Mehreteab A. Effect of nonionic admixtures on the adsorption of ionic surfactants at fluid interfaces. 1. Sodium dodecyl sulfate and dodecanol. Langmuir 2003;19:5004–18.
[77] Lianos P, Zana R. Fluorescence probe studies of the effect of concentration on the state of aggregation of surfactants in aqueous solution. J Colloid Interface Sci 1981;84:100–7.
[78] Mondain-Monval O, Leal-Calderon F, Bibette J. Forces between emulsion droplets: role of surface charges and excess surfactant. J Phys II France 1995;6:1313–29.
[79] Zana R, Lévy H, Danino D, Talmon Y, Kwetkat K. Mixed micellization of cetyltrimethylammonium bromide and an anionic dimeric (gemini) surfactant in aqueous solution. Langmuir 1997;13:402–8.
[80] Adamczyk Z, Para G, Warszyski P. Influence of ionic strength on surface tension of cetyltrimethylammonium bromide. Langmuir 1999;5:8383–7.
[81] Bain CD, Manning-Benson S, Darton RC. Rates of mass transfer and adsorption of hexadecyltrimethylammonium bromide at an expanding air–water interface. J Colloid Interface Sci 2000;229:247–56.
[82] Chakraborty T, Ghosh S, Moulik SP. Micellization and related behavior of binary and ternary surfactant mixtures in aqueous medium: cetylpyridinium chloride (CPC), cetyltrimethylammonium bromide (CTAB), and polyoxyethylene (10) cetyl ether (Brij-56) derived system. J Chem Phys B 2005;109:14813–23.
[83] Modaressi A, Sifaoui H, Grzesiak B, Solimando R, Domanska U, Rogalski M. CTAB aggregation in aqueous solutions of ammonium based ionic liquids; conductimetric studies. Colloids Surf A 2007;296:104–8.
[84] Javadian S, Gharibi H, Bromand Z, Sohrabi B. Electrolyte effect on mixed micelle and interfacial properties of binary mixtures of cationic and nonionic surfactants. J Colloid Interface Sci 2008;318:449–56.
[85] Hassan PA, Hodgdon TK, Sagasaki M, Fritz-Popovski G, Kaler EW. Phase behavior and microstructure evolution in aqueous mixtures of cetyltrimethylammonium bromide and sodium dodecyl tri-oxyethylene sulfate. CR Chim 2009;12:18–29.
[86] García-Río L, Leis JR, Mejuto JC, Mosquera V, Rodríguez-Dafonte P. Stability of mixed micelles of cetylpyridinium chloride and linear primary alkylamines. Colloids Surf A 2007;309:216–23.
[87] Mukhim T, Ismail K. Micellization of cetylpyridinium chloride in aqueous lithium chloride, sodium chloride, and potassium chloride media. J Surf Sci Technol 2005;21:113–27.
[88] Varade D, Joshi T, Aswal VK, Goyal PS, Hassan PA, Bahadur P. Effect of salt on the micelles of cetylpyridinium chloride. Colloids Surf A 2005;259:95–101.
[89] Chatterjee A, Moulik SP, Sanyal SK, Mishra BK, Puri PM. Thermodynamics of micelle formation of ionic surfactants: a critical assessment for sodium dodecyl sulfate, cetylpyridinium chloride and dioctyl sulfosuccinate (Na salt) by microcalorimetric, conductometric, and tensiometric measurements. J Phys Chem B 2001;105:12823–31.
[90] Amos DA, Lynn S, Radke CJ. A self-consistent multicomponent activity coefficient model for ionic micellar surfactant solutions. Langmuir 1998;14:2297–306.
[91] Choudhary VR, Nayak VC, Choudhary TV. Single-component sorption/diffusion of cyclic compounds from their bulk liquid phase in H-ZSM-5 zeolite. Ind Eng Chem Res 1997;36:1812–8.
[92] Scheludko A, Exerowa D. Instrument for interferometric measuring of the thickness of microscopic foam films. C R Acad Bulg Sci 1959;7:123–32.
[93] Sheludko A. Thin liquid films. Adv Colloid Interface Sci 1967;1:391–464.
[94] Vautier-Giongo C, Bales BL. Estimate of the ionization degree of ionic micelles based on Krafft temperature measurements. J Phys Chem B 2003;107:5398–403.
[95] Feinstein ME, Rosano HL. The determination of the apparent binding of counterions to micelles by electromotive force measurements. J Colloid Interface Sci 1967;24:73–9.
[96] Corrin ML, Harkins WD. The effect of salts on the critical concentration for the formation of micelles in colloidal electrolytes. J Am Chem Soc 1947;69:683–8.
[97] Corrin ML. The effect of salts and chain length on the critical concentration of colloidal electrolytes. J Colloid Sci 1948;3:333–8.
[98] Kolev VL, Danov KD, Kralchevsky PA, Broze G, Mehreteab A. Comparison of the van der Waals and Frumkin adsorption isotherms for sodium dodecyl sulfate at various salt concentrations. Langmuir 2002;18:9106–9.
[99] Kralchevsky PA, Danov KD, Broze G, Mehreteab A. Thermodynamics of ionic surfactant adsorption with account for the counterion binding: effect of salts of various valency. Langmuir 1999;15:2351–65.
[100] Valkovska DS, Shearman GC, Bain CD, Darton RC, Eastoe J. Adsorption of ionic surfactants at an expanding air–water interface. Langmuir 2004;20:4436–45.
[101] Taylor CD, Valkovska DS, Bain CD. A simple and rapid method for the determination of the surface equations of state and adsorption isotherms for efficient surfactants. Phys Chem Chem Phys 2003;5:4885–91.
[102] Para G, Jarek E, Warszynski P. The Hofmeister series effect in adsorption of cationic surfactants — theoretical description and experimental results. Adv Colloid Interface Sci 2006;122:39–55.
[103] Ivanov IB, Marinova KG, Danov KD, Dimitrova D, Ananthapadmanabhan KP, Lips A. Role of the counterions on the adsorption of ionic surfactants. Adv Colloid Interface Sci 2007;134–135:105–24.
[104] Miyata I, Takada A, Yonese M, Kishimoto H. Solution behavior of sodium dodecyl sulfate in methanol. Bull Chem Soc Jpn 1990;63:3502–7.
[105] Gunaseelan K, Ismail K. Estimation of micellization parameters of sodium dodecyl sulfate in water + 1-butanol using the mixed electrolyte model for molar conductance. J Colloid Interface Sci 2003;258:110–5.
[106] Durand-Vidal S, Turq P, Bernard O, Treiner C. Model for the conductivity of ionic mixtures in the mean spherical approximation. 2. Surfactant solutions. J Phys Chem B 1997;101:1713–7.
[107] Kim D-H, Oh S-G, Park Y-C, Chang Y-H. Effect of cesium and sodium ions on interfacial tension of hexadecane/aqueous dodecyl sulfate solutions. J Ind Eng Chem 2000;6:188–93.
[108] Herrington KL, Kaler EW, Miller DD, Zasadzinski JA, Chiruvolu S. Phase behavior of aqueous mixtures of dodecyltrimethylammonium bromide (DTAB) and sodium dodecyl sulfate (SDS). J Phys Chem 1993;97:13792–802.

[109] Neves ACS, Valente AJM, Burrows HD, Ribeiro ACF, Lobo VMM. Effect of terbium (III) chloride on the micellization properties of sodium decyl- and dodecylsulfate solutions. J Colloid Interface Sci 2007;306:166–74.
[110] Bakshi MS, Kaura A, Miller JD, Paruchuri VK. Sodium dodecyl sulfate-poly (amidoamine) interactions studied by AFM imaging, conductivity, and Krafft temperature measurements. J Colloid Interface Sci 2004;278:472–7.
[111] Vautier-Giongo C, Pastore HO. Micellization of CTAB in the presence of silicate anions and the exchange between bromide and silicate at the micelle surface: a step to understand the formation of mesoporous molecular sieves at extremely low surfactant and silicate concentrations. J Colloid Interface Sci 2006;299:874–82.
[112] Kuperkar K, Abezgauz L, Prasad K, Bahadur P. Formation and growth of micelles in dilute aqueous CTAB solutions in the presence of $NaNO_3$ and $NaClO_3$. J Surfactants Deterg 2010;13:293–303.
[113] Graciani MM, Muñoz M, Rodrígues A, Moyá ML. Water-n, n-dimethylformamide alkyltrimethylammonium bromide micellar solutions: thermodynamic, structural, and kinetics studies. Langmuir 2005;21:3303–10.
[114] Kralchevsky PA, Boneva MP, Danov KD, Ananthapadmanabhan KP, Lips A. Method for analysis of the composition of acid soaps by electrolytic conductivity measurements. J Colloid Interface Sci 2008;327:169–79.
[115] Boneva MP, Danov KD, Kralchevsky PK, Kralchevska SD, Ananthapadmanabhan KP, Lips A. Coexistence of micelles and crystallites in solutions of potassium myristate: soft matters vs. solid matters. Colloids Surf A 2010;354:172–87.
[116] Harned HS, Owen BB. The physical chemistry of electrolytic solutions. 2nd ed. New York: Reinhold Publishing Corp; 1950.
[117] Ravdel AA, Ponomareva AM, editors. Concise handbook of physiochemical quantities. Eighth ed. Leningrad: Khimiya; 1983. [in Russian].
[118] Robinson RA, Stokes RH. Electrolyte solutions. London: Butterworth; 1959.
[119] Bunton CA, Romsted LS, Sepulveda L. A quantitative treatment of micellar effects upon deprotonation equilibriums. J Phys Chem 1980;84:2611–8.
[120] Dorshow R, Briggs J, Bunton CA, Nicoli DF. Dynamic light scattering from cetyltrimethylammonium bromide micelles. Intermicellar interactions at low ionic strengths. J Phys Chem 1982;86:2388−2395–2388−.
[121] Sepulveda L, Cortes J. Ionization degrees and critical micelle concentrations of hexadecyltrimethylammonium and tetradecyltrimethylammonium micelles with different counterions. J Phys Chem 1985;89:5322–4.
[122] Mitaku S, Ohtsuki T, Enari K, Kishimoto A, Okano K. Studies of ordered monodisperse polystyrene latexes. I. Shear ultrasonic measurements. Jpn J Appl Phys 1978;17:305–13.
[123] Ohtsuki T, Mitaku S, Okano K. Studies of ordered monodisperse polystyrene latexes. II. Theory of mechanical properties. Jpn J Appl Phys 1978;17:627–35.
[124] Alexander S, Chaikin PM, Grant P, Morales GJ, Pincus P. Charge renormalization, osmotic pressure, and bulk modulus of colloidal crystals: theory. J Chem Phys 1984;80:5776–81.
[125] Groot RD. Ion condensation on solid particles: theory and simulations. J Chem Phys 1991;95:9191–203.
[126] Landau LD, Lifshitz E. Electrodynamics of continuous medium. Oxford: Pergamon Press; 1960.
[127] Derjaguin BV, Churaev NV, Muller VM. Surface forces. New York: Plenum Press; 1987.
[128] Derjaguin BV. Theory of stability of colloids and thin liquid films. New York: Plenum Press; 1989.
[129] Kirkwood JG, Oppenheim I. Chemical thermodynamics. New York: McGraw-Hill; 1961.
[130] Lai SK, Wang GF. Ergodic–nonergodic phase diagram for a concentrated suspension of charge-stabilized colloids: rescaled mean spherical approximation. Phys Rev E 1998;58:3072–82.
[131] Lai SK, Wang JL, Wang GF. Static structure factor of a suspension of charge-stabilized colloids: application to liquid–glass transition phase diagram and to micellar solution. J Chem Phys 1999;110:7433–42.
[132] Banchio AJ, Nägele G. Short-time transport properties in dense suspensions: from neutral to charge-stabilized colloidal spheres. J Chem Phys 2008;128: 104903.
[133] Gapinski J, Patkowski A, Banchio AJ, Buitenhuis J, Holmqvist P, Lettinga MP, Meier G, Nägele G. Structure and short-time dynamics in suspensions of charged silica spheres in the entire fluid regime. J Chem Phys 2009;130:084503.
[134] Zoetekouw B, van Roij R. Volume terms for charged colloids: a grand-canonical treatment. Phys Rev E 2006;73:021403.
[135] Castañeda-Priego R, Rojas-Ochoa LF, Lobaskin V, Mixteco-Sánchez JC. Macroion correlation effects in electrostatic screening and thermodynamics of highly charged colloids. Phys Rev E 2006;74:051408.
[136] Trizac E, Belloni L, Dobnikar J, von Grünberg HH, Castañeda-Priego R. Macroion virial contribution to the osmotic pressure in charge-stabilized colloidal suspensions. Phys Rev E 2007;75:011401.
[137] Rojas-Ochoa LF, Castañeda-Priego R, Lobaskin V, Stradner A, Scheffold F, Schurtenberger P. Density dependent interactions and structure of charged colloidal dispersions in the week screening regime. Phys Rev Lett 2008;100:178304.
[138] Rojas LF, Urban G, Schurtenberger P, Gisler T, von Grünberg HH. Reappearance of structure in colloidal suspensions. EPL-Europhys Lett 2002;60:802–8.
[139] Haro-Pérez C, Quesada-Pérez M, Callejas-Fernández J, Sabaté R, Estelrich J, Hidalgo-Álvarez R. Probing the jellium model with colloidal dispersions of charged liposomes. Colloids Surf A 2005;270:352–6.
[140] Dobnikar J, Castañeda-Priego R, von Grünberg HH, Trizac E. Testing the relevance of effective interaction potentials between highly-charged colloids in suspension. New J Phys 2006;8:277.
[141] Safran SA, Pincus PA, Cates ME, MacKintosh FC. Growth of charged micelles. J Phys France 1990;51:503–10.
[142] Löwen H, Madden PA, Hansen J-P. Ab initio description of counterion screening in colloidal suspensions. Phys Rev Lett 1992;68:1081–4.
[143] Diehl A, Barbosa MC, Levin Y. Charge renormalization and phase separation in colloidal suspensions. EPL-Europhys Lett 2001;53:86–92.
[144] Trizac E, Bocquet L, Aubouy M. Simple approach for charge renormalization in highly charged macroions. Phys Rev Lett 2002;89:248301.
[145] Trizac E, Bocquet L, Aubouy M, von Grünberg HH. Alexander's prescription for colloidal charge renormalization. Langmuir 2003;19:4027–33.
[146] Henle ML, Santangelo CD, Patel DM, Pincus PA. Distribution of counterions near discretely charged planes and rods. EPL-Europhys Lett 2004;66:284–90.
[147] Diehl A, Levin Y. Effective charge of colloidal particles. J Chem Phys 2004;121:12100–3.
[148] Téllez G, Trizac E. Nonlinear screening of spherical and cylindrical colloids: the case of 1:2 and 2:1 electrolytes. Phys Rev E 2004;60:011404.
[149] Chapot D, Bocquet L, Trizac E. Electrostatic potential around charged finite rodlike macromolecules: nonlinear Poisson–Boltzmann theory. J Colloid Interface Sci 2005;285:609–18.
[150] Crocker JC, Grier DG. Microscopic measurement of the pair interaction potential of charge-stabilized colloid. Phys Rev Lett 1994;73:352–5.
[151] Bitzer F, Palberg T, Löwen H, Simon R, Leiderer P. Dynamical test of interaction potentials for colloidal suspensions. Phys Rev E 1994;50:2821–6.
[152] Allahyarov E, Löwen H, Trigger S. Effective forces between macroions: the case of asymmetric macroions and added salt. Phys Rev E 1998;57:5818–24.
[153] Goulding D, Hansen J-P. Attraction between like-charged colloidal particles induced by a surface: a density-functional analysis. EPL-Europhys Lett 1999;46:407–13.
[154] Denton AR. Effective interactions and volume energies in charged colloids: linear response theory. Phys Rev E 2000;62:3855–64.
[155] Lau AWC, Pincus P, Levine D, Fertig HA. Electrostatic attraction of coupled Wigner crystals: finite temperature effect. Phys Rev E 2001;63:051604.
[156] Denton AR, Löwen H. Stability of colloidal quasicrystals. Phys Rev Lett 1998;81:469–72.
[157] Levin Y, Barbosa MC, Tamashiro MN. Liquid-state theory of charged colloids. EPL-Europhys Lett 1998;41:123–7.
[158] Shklovskii BI. Screening of a macroion by multivalent ions: correlation-induced inversion of charge. Phys Rev E 1999;60:5802–11.
[159] Diehl A, Levin Y. Smoluchowski equation and colloidal charge reversal. J Chem Phys 2006;125:054902.
[160] Kreer T, Horbach J, Chatterji A. Nonlinear effects in charge stabilized colloidal suspensions. Phys Rev E 2006;74:021401.
[161] Denton AR. Electroneutrality and phase behavior of colloidal suspensions. Phys Rev E 2007;76:051401.
[162] Trizac E, Hansen J-P. A Wigner–Seitz model of charged lamellar colloidal dispersions. Phys Rev E 1997;56:3137–49.
[163] Leote de Carvalho RJF, Trizac E, Hansen J-P. Nonlinear Poisson–Boltzmann theory of a Wigner–Seitz model for swollen clays. Phys Rev E 2000;61:1634–47.
[164] Levin Y, Diehl A, Fernández-Nieves A, Fernández-Barbero A. Thermodynamics of ionic microgels. Phys Rev E 2002;65:036143.
[165] Gisler T, Schulz SF, Borkovec M, Sticher H, Schurtenberger P, D'Aguanno B, Klein R. Understanding colloidal charge renormalization from surface chemistry: experiment and theory. J Chem Phys 1994;101:9924–36.
[166] Tamashiro MN, Schiessel H. Where the linearized Poisson–Boltzmann cell model fails: spurious phase separation in charged colloidal suspensions. J Chem Phys 2003;119:1855–65.
[167] Denton AR. Poisson–Boltzmann theory of charged colloids: limits of the cell model for salty suspensions. J Phys Condens Matter 2010;22:364108.
[168] Reiss-Husson F, Luzzati V. The structure of the micellar solutions of some amphiphilic compounds in pure water as determined by absolute small-angle X-ray scattering techniques. J Phys Chem 1964;68:3504–11.
[169] Van Stam J, Depaemelaere S, De Schryver FC. Micellar aggregation numbers — a fluorescence study. J Chem Educ 1998;75:93–8.
[170] Toshev BV, Ivanov IB. Thermodynamics of thin liquid films. I. Basic relations and conditions for equilibrium. Colloid Polym Sci 1975;253:558–65.
[171] Derjaguin BV, Landau LD. Theory of the stability of strongly charged lyophobic sols and of the adhesion of strongly charged particles in solutions of electrolytes. Acta Physicochim URS 1941;14:633–62.
[172] Verwey EJW, Overbeek JThG. Theory of the stability of lyophobic colloids. Amsterdam: Elsevier; 1948.
[173] Russel WB, Saville DA, Schowalter WR. Colloidal dispersions. Cambridge: Cambridge Univ. Press; 1989.
[174] Langmuir I. The role of attractive and repulsive forces in the formation of tactoids, thixotropic gels, protein crystals and coacervates. J Chem Phys 1938;6:873–96.
[175] Hill TL. An introduction to statistical thermodynamics. New York: Dover Publications; 1987.
[176] Adamczyk Z, Weronski P. Kinetics of irreversible adsorption of interacting spheroidal particles. Langmuir 1995;11:4400–10.
[177] Adamczyk Z, Warszynski P. Role of electrostatic interactions in particle adsorption. Adv Colloid Interface Sci 1996;63:41–149.
[178] Semmler M, Mann EK, Rička J, Borkovec M. Diffusional deposition of charged latex particles on water–solid interfaces at low ionic strength. Langmuir 1998;14:5127–32.
[179] Semmler M, Rička J, Borkovec M. Diffusional deposition of colloidal particles: electrostatic interaction and size polydispersity effect. Colloids Surf A 2000;165:79–93.
[180] Hughes RIG. Theoretical practice: the Bohm–Pines quartet. Perspectives Sci 2006;14:457–524, doi:10.1162/posc.2006.14.4.457.
[181] Keller HB. A new finite difference scheme for parabolic problems. In: Hubbard B, editor. Numerical solutions of partial differential equations II. SYNSPADE 1970. New York: Academic Press; 1971. p. 327–50.
[182] Morton KW, Mayers DF. Numerical solutions of partial differential equations. Cambridge: Cambridge University Press; 2005.